Monthly Notices
of the
ROYAL ASTRONOMICAL SOCIETY

MNRAS **440,** 1391–1409 (2014)
Advance Access publication 2014 March 23

doi:10.1093/mnras/stu296

The candidate luminous blue variable G79.29+0.46: a comprehensive study of its ejecta through a multiwavelength analysis

C. Agliozzo,[1,2]★ A. Noriega-Crespo,[3] G. Umana,[4] N. Flagey,[5] C. Buemi,[4] A. Ingallinera,[4] C. Trigilio[4] and P. Leto[4]

[1]*Departamento de Ciencias Fisicas, Universidad Andres Bello, Avda. Republica 252, Santiago, Chile*
[2]*Dipartimento di Fisica e Astronomia, Sezione Astrofisica, Università degli studi di Catania, via S. Sofia 64, I-95123, Catania, Italy*
[3]*Infrared Processing and Analysis Center, California Institute of Technology, 1200 East California Boulevard, Pasadena, CA 91125, USA*
[4]*INAF Osservatorio Astrofisico di Catania, via S. Sofia 78, I-95123, Catania, Italy*
[5]*Jet Propulsion Laboratory, California Institute of Technology, 4800 Oak Grove Drive, Pasadena, CA 91109, USA*

Accepted 2014 February 10. Received 2014 February 7; in original form 2013 November 23

ABSTRACT

We present a multiwavelength analysis of the nebula around the candidate luminous blue variable G79.29+0.46. The study is based on our radio observations performed at the Expanded Very Large Array and at the Green Bank Telescope and on archival infrared data sets, including recent images obtained by the *Herschel Space Observatory*. We confirm that the radio central object is characterized by a stellar wind and we derive a current mass-loss rate of about $1.4 \times 10^{-6}\,M_{\odot}\,yr^{-1}$. We find the presence of a dusty compact envelope close to the star, with a temperature between ∼40 and 1200 K. We estimate for the outer ejecta an ionized gas mass of $1.51\,M_{\odot}$ and a warm (60–85 K) dust mass of $0.02\,M_{\odot}$. Diagnostics of the far-infrared spectra indicate the presence of a photodissociation region around the ionized gas. Finally, we model the nebula with the photoionization code CLOUDY, using as input parameters those estimated from our analysis. We find for the central star a luminosity of $10^{5.4}\,L_{\odot}$ and an effective temperature of 20.4 kK.

Key words: stars: early-type – stars: evolution – stars: mass-loss – ISM: bubbles – infrared: ISM – radio continuum: ISM.

1 INTRODUCTION

Evolved luminous stars with an initial mass more than $20\,M_{\odot}$ are believed to enter an instability phase, historically known as the luminous blue variable (LBV) phase. This phase is characterized by intense mass-loss rates ($\sim 10^{-5}$–$10^{-3}\,M_{\odot}\,yr^{-1}$), associated with visual/near-infrared (NIR) spectroscopic and photometric variabilities (Humphreys & Davidson 1994), before the star evolves as a Wolf–Rayet (WR) star, once it has reduced its mass (Conti & Frost 1976). However, the occurrence of this phase during the evolution of massive stars and the mass-loss mechanism are still not well understood, mostly because of the rarity of LBVs in our Galaxy. At present, there are only 12 objects in the Milky Way that satisfy the variability criteria coupled with high mass-loss rates. However, recently the number of candidate LBVs (cLBVs) has increased to 55 (Humphreys & Davidson 1994; van Genderen 2001; Clark, Larionov & Arkharov 2005; Gvaramadze, Kniazev & Fabrika 2010; Wachter et al. 2011; Nazé, Rauw & Hutsemékers 2012), based on the discovery of ring nebulae surrounding these luminous stars. In fact, as a result of the mass loss, such evolved massive stars can be surrounded by circumstellar nebulae, rich in processed material (Lamers et al. 2001). So far, LBV nebulae (LBVNe) have been observed in about 20 objects among LBVs and cLBVs in our Galaxy, and they have shown to be dusty, hence emitting in a wide spectral domain. Such nebulae are indeed the fingerprints of the mass-loss phenomenon, and therefore multiwavelength observations provide unique insights into the LBV mass-loss history.

The importance of studying LBVNe is increased by the possibility that they can skip the WR stage and experience an explosive supernova (SN) event (e.g. Kotak & Vink 2006; Vink, de Koter & Kotak 2008a; Van Dyk 2013). If this is true, the LBV mass-loss phenomenon is also of great interest for the study of Type IIn SNe, whose evolution is influenced by the circumstellar material originated through the mass loss of the progenitor star (Chugai & Danziger 2003; Smith et al. 2007; Ofek et al. 2013). Therefore, the mass-loss archaeology appears to be fundamental for different aspects of the evolution of massive stars.

In this paper, we propose a new study of the ejecta around G79.29+0.46, a galactic cLBV located in Cygnus-X ($D \sim 1.7$ kpc; Schneider et al. 2006), one of the richest star-forming regions in our Galaxy. Because of its location and also because of its beautiful aspect and intriguing nature, this star and its associated nebula have been widely observed in spectral domains ranging from

★ E-mail: agliozzo@oact.inaf.it

the optical to the radio. These observations have made it possible to investigate different components of the ejecta associated with G79.29+0.46, which has been shown to have lost mass with different events (Jiménez-Esteban, Rizzo & Palau 2010; Kraemer et al. 2010). Diverse works focused on this source can be mentioned (e.g. Higgs, Wendker & Landecker 1994; Waters et al. 1996; Voors et al. 2000a; Rizzo, Jiménez-Esteban & Ortiz 2008; Umana et al. 2011, hereafter Paper I), but a comprehensive study of the star and its associated nebula has not yet been performed. Moreover, the physical parameters determined in these works are often based on different assumptions, making their comparison and interpretation difficult. For instance, Higgs et al. (1994) interpreted the ring-like shell around the star as interstellar material swept up by the stellar wind and estimated for this shell a mass of about 14–15 $M_{\odot}$. Later, the nebula was recognized as ejecta associated with the star (Waters et al. 1996), but a reappraisal of its properties has still to be carried out. The nebular mass inferred by Higgs et al. (1994) and Waters et al. (1996) suggests that the nebula associated with G79.29+0.46 is amongst the most massive known (see table 9 of Clark et al. 2003). If correct, the mass would rival that of the Homunculus around η Carina (e.g. Morris et al. 1999; Smith et al. 2003), but the central star of G79.29+0.46 is likely to be over an order of magnitude fainter (about $10^{5.5}$ $L_{\odot}$, while η Car is $10^{6.7}$ $L_{\odot}$; Higgs et al. 1994; Voors et al. 2000a; Hillier et al. 2001) and consequently far less massive. Therefore, the nebular mass would represent a higher proportion of its initial mass.

In this paper, we propose a new analysis of the multiple components of the nebula around G79.29+0.46, using recent observations, which we performed in the radio domain, new far-infrared (FIR) images provided by the *Herschel Space Observatory* and other archival FIR and mid-IR spectroscopic and photometric data sets collected in the last 20 yr by different telescopes. The main assumption in this work is that the photometric and spectroscopic properties of this star have not changed significantly in the considered time lapse, a hypothesis reinforced by the fact that G79.29+0.46 is still a cLBV, because no significant visual or NIR variability has been observed so far (Voors et al. 2000a; Vink et al. 2008b).

This work started with our observations of G79.29+0.46 performed at the Expanded Very Large Array (EVLA). The preliminary results of these observations were presented in Paper I, and the highest resolution radio image was compared with the *Spitzer* IR images. This revealed that the multiple shells around the star have signatures of different populations of dust and that the radio emission is ionization bounded. In this paper, we complement the preliminary work in Paper I with new radio observations performed at the Green Bank Telescope (GBT) in order to overcome the typical problem of interferometers (i.e. zero baseline missing), which makes it impossible to determine the total flux of extended sources. Therefore, we propose a new analysis of the radio emission aimed at determining important physical parameters related to the ionized gas and to the central star. We also perform an analysis of the IR data sets retrieved from the data archives, in order to determine IR lines and physical properties related to the dust component.

The paper is organized as follows. In Section 2, we describe our observations and the archival data sets considered in this study. Then, we present our analysis of the radio data sets (Section 3), focused on the ionized gas distribution and emission, while in Section 4 we study the dust emission and properties, probed by the IR images. Section 5 concerns the spectroscopic mid-IR and FIR analysis of the nebula. In Section 6, we present a simple model obtained with the photoionization code CLOUDY. We conclude with a brief description of the star's mass-loss history in Section 7.

2 DATA SETS

2.1 Radio observations and data processing

We performed high-resolution and high-sensitivity observations of G79.29+0.46 at 20 and 6 cm (1.4 and 5 GHz, respectively) using the EVLA in configurations D and C. These observations and the data reduction process have already been described in Paper I, where we presented only the final map at 6 cm obtained by concatenating the *uv* data sets in both configurations D and C. Here we describe the imaging process for each data set.

The calibrated visibilities were imaged by adopting a natural weighting scheme and using the Clark algorithm for the dirty image deconvolution. Thus, the cleaned images were convolved with a two-dimensional Gaussian, with the half power beam width (HPBW) reported in Table 1. Following this scheme, we have obtained four maps. For each frequency, we also concatenated data obtained in the two array configurations D and C, in order to increase the *uv* coverage. Therefore, we imaged the new data sets. Peak flux density (on-source) and the rms noise are listed in Table 1 for all the maps. We also report the largest angular scale (LAS) achieved with the proposed array configurations.

To complement the interferometric data sets, single-dish observations of G79.29+0.46 were carried out at the GBT at 1.4 and 5 GHz in 2011 June as a part of a project including a sample of galactic circumstellar shells (Ingallinera et al., in preparation). The observations were performed by running 30 scans on both RA and Dec. directions for a final field of view (FOV) of 1 deg 15 arcmin at 1.4 GHz and 25 arcmin at 5 GHz. The data reduction, consisting of basic calibration and imaging, has been performed using the IDL routine `topsi` provided by the GBT staff. However, the images were affected by stripes, systematic errors resulting from instrumental drifts that shift the base level of each scan. Therefore, the images were destriped using an appropriate filter in the

Table 1. Properties of the interferometric radio maps.

Configuration and frequency	HPBW (arcsec)^2	PA (deg)	LAS (arcsec)	Peak on-source (mJy beam^{-1})	rms (mJy beam^{-1})
EVLA:D, 1.391 GHz	50.40 × 42.83	163.6	129	26.0	2
EVLA:D, 4.959 GHz	16.46 × 14.16	−33.2	88	6.8	0.7
EVLA:C, 1.391 GHz	27.72 × 14.44	44.4	258	9.6	2.5
EVLA:C, 4.959 GHz	9.41 × 4.84	58.7	124	2.11	0.18
EVLA:D+C, 1.391 GHz	26.84 × 24.65	36.1	129	13.17	1.1
EVLA:D+C, 4.959 GHz	4.56 × 3.09	101.16	124	1.76	0.07
VLA:D+C, 8.46 GHz	6.25 × 3.12	57.3	164	1.68	0.15

Table 2. Properties of the GBT and GBT&EVLA radio maps.

Configuration and frequency	HPBW (arcsec)^2	PA (deg)	FOV (arcsec)	Peak on-source (mJy beam^{-1})	Std dev. (mJy beam^{-1})
GBT, 5.100 GHz	144 × 144	0	1500	14.27×10^3	12.43
GBT&EVLA:D+C, 4.959 GHz	4.56 × 3.09	101.16	1500	3.22	0.06

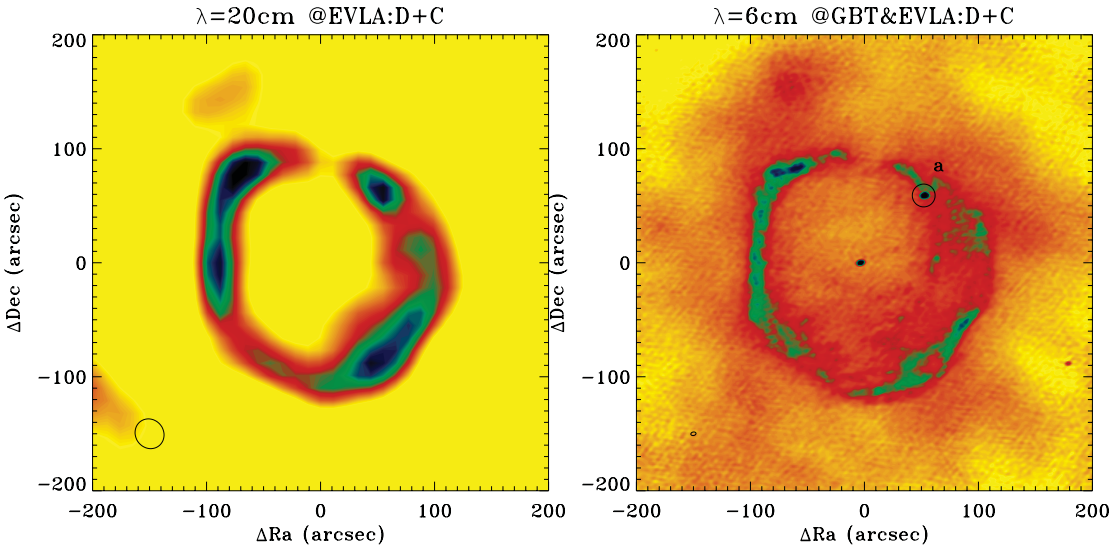

Figure 1. Final radio maps obtained in this work: left, EVLA:D+C 20-cm (1.4-GHz) map; right, 6-cm (5-GHz) map after combining the GBT and EVLA images. In the bottom-left corner of each map, the synthetic beam is shown (i.e. the resolution in the map). In the right panel, the object marked by 'a' is an extragalactic object, first detected by Higgs et al. (1994).

Fourier domain (Emerson & Graeve 1988; Ingallinera et al., in preparation). Unfortunately, at 1.4 GHz, the beam of the telescope is about four times larger than the nebula size, and as a result the sensitivity is limited by confusion. Therefore, we complement the interferometric map with the single-dish map only at 5 GHz, as in the following.

The 5-GHz GBT map was rescaled to the EVLA map units (i.e. converted from the unit of antenna temperature T_A to Jy beam^{-1}) by using the GBT antenna gain $G = 2.84\ \eta_A$, with the antenna efficiency $\eta_A = 0.72$,[1] valid at 5 GHz. The GBT map was then rescaled to the central frequency of the EVLA data (the GBT central frequency is 5.100 GHz and that of the EVLA is 4.959 GHz). This conversion was performed by assuming that the emission is almost a result of optically thin free–free transitions ($\alpha = -0.1$), an assumption confirmed in Section 3.2 by analysing the spectral index from the EVLA maps. The resulting flux density peak in the 5-GHz GBT map is shown in Table 2. In the map, because the background emission is high, the rms does not give a good estimation of the noise. Hence, in Table 2 we provide the standard deviation (std dev.). The new single-dish map was then imported into the CASA package (version 4.2) and processed together with the EVLA map at 5 GHz, by using the recently improved task `feather`, which combines two images with different spatial resolutions. In this procedure, the single-dish flux scale was not modified (`sdfactor` = 1) and the effective single-dish diameter was set to 100 m.

The final map at 5 GHz is shown in Fig. 1, together with that at 1.4 GHz. In the 5-GHz map, the peak flux density corresponds to the point source projected on the nebula in the north-west direction (object 'a'). The map is filled with diffuse emission arising from the close H II region in the south of G79.29+0.46 (e.g. see fig. 1 of Higgs et al. 1994). As a result, there are no regions free of emission where we can properly evaluate the rms in the map. Therefore, we again approximate the noise as the standard deviation (Table 2). For the analysis of the radio emission (Section 3), the background contribution is subtracted from the map.

Exploring the VLA data archives, we found further observations of G79.29+0.46 at 8.46 GHz. These observations were performed in 2005 May and August, using configurations C and B (P.I. C. Lang) in continuum mode. We have retrieved these data sets and calibrated them by adopting the same procedure used for the EVLA:D+C data. Properties of the final map are summarized in Table 1.

2.2 Archival infrared data sets

In order to study the different emitting components in the nebula around G79.29+0.46, we have retrieved most of the spectroscopic and photometric data from the mid-IR to FIR present in the archives. The considered data sets are summarized in Tables 3 and 4, which include data collected with the *Herschel Space Observatory*, the *Spitzer* Space Telescope, the *Infrared Space Observatory* (*ISO*), the *Infrared Astronomical Satellite* (*IRAS*) and the *Wide-field Infrared Survey Explorer* (*WISE*). In Table 4, we also indicate the wavelength and the full width at half-maximum (FWHM) for each data set.

The *Herschel* images come from the *Herschel* imaging survey of OB young stellar objects (HOBYS; P.I. F. Motte) and from the mass-loss of evolved stars (MESS; P.I. M. A. T. Groenewegen) programmes, which used the photodetecting array camera and spectrometer (PACS) and the spectral and photometric imaging receiver

[1] See the observing manual for the GBT at http://www.gb.nrao.edu/gbtprops/man/GBTpg.pdf.

Table 3. Summary of archival spectroscopic data and instrument properties.

Telescope	Instrument	λ (μm)	FOV (arcsec)^2	Project ID
Spitzer	IRS/SL	5.2–14.5	3.6 × 57	17333-248/504[a]
Spitzer	IRS/SH	9.9–19.6	4.7 × 11.3	17333-248/504[a]
ISO	SWS06	12.2–13.2	27 × 14	69200901
ISO	SWS06	17–27; 30–34	33 × 20	76802901
Spitzer	IRS/LH	18.7–37.2	11.1 × 22.3	17333-248/504[a]
ISO	SWS06	34–35	33 × 20	51705105
ISO	LWS02	41.14–178.75	84 × 84	358010-03/05/07/ 358010-08/11/14

[a] ON and OFF nebula observations, respectively.

Table 4. Summary of archival photometric data and instrument properties.

Telescope	Instrument	λ (μm)	FWHM (arcsec)	Project ID
ISO	CAM01	8.69	3	35700630
ISO	CAM01	12.41	4.3	35700630
WISE	W3	12	6	*WISE* Survey
ISO	CAM01	13.53	4.7	35700630
WISE	W4	22	12	*WISE* Survey
Spitzer	MIPS	24	6	22508544
IRAS	HiRES	60	60	*IRAS* Survey
Herschel	PACS	70	5.5	1342244-168/169
Spitzer	MIPS	70	18	22508544
Herschel	PACS	100	6.7	1342196-767/768
Herschel	PACS	160	11	1342196-769/770
Herschel	SPIRE	250	18	1342187718
Herschel	SPIRE	350	25	1342187718
Herschel	SPIRE	500	37	1342187718

(SPIRE). The PACS photometric data (from MESS) include the 100-μm data, while the SPIRE/PACS parallel observations (HOBYS) provide the 70-, 160-, 250-, 350- and 500-μm data. The *Herschel* images are presented here for the first time, as well as the *WISE* (Wright et al. 2010) data (which come from the Image Atlas), while the multiband imaging photometer (MIPS) maps have already been published (Jiménez-Esteban et al. 2010; Kraemer et al. 2010; Paper I). The *ISO* images were briefly discussed in the poster paper of Trams, Voors & Waters (1998) and those of the *IRAS* (obtained with HIRES) by Higgs et al. (1994) and Waters et al. (1996).

From the *ISO* data archive, we also retrieved the spectroscopic data sets (see Table 3). The long wavelength spectrometer (LWS) spectra were presented by Wendker et al. (1998), but they provided only a qualitative discussion of the data. The short wavelength spectrometer (SWS) spectra appeared for the first time in Morris et al. (2008). The infrared spectrograph (IRS) spectra were acquired with the short–low (SL), short–high (SH) and long–high (LH) modules. These data have already been analysed by Jiménez-Esteban et al. (2010), but, despite the interesting study proposed, they did not consider the off-nebula data set. Hence, they did not subtract the background, which strongly affects the target continuum and line emissions. Moreover, they did not apply corrections for extinction in their diagnostic study. Thus, we propose a new analysis. The positions of the IRS, SWS and LWS slits projected on to the nebula around G79.29+0.46 are shown in the Appendix (see Figs A1 and A2).

3 ANALYSIS OF THE RADIO CONTINUUM EMISSION

3.1 Morphology and analysis of the ionized gas

The map at 1.4 GHz shows that the emission arises mostly from the nebula (see the left panel of Fig. 1). The central object is not detected for two possible reasons: (1) because the spectral index of stellar winds ($\alpha \sim 0.6$) implies low flux density at low frequencies; (2) because of the confusion limit of the interferometer at this frequency. The spur-emission in the north-east of the nebula – first noticed by Higgs et al. (1994) – is visible. At 5 GHz, it is possible to distinguish the emission from a compact central object, as well as that from the nebula and from the spur (Fig. 1, right panel). As already discussed in Paper I, the highest resolution maps (at 5 GHz) reveal a highly structured texture of the nebula and the extragalactic source overlaid on the nebula in the north-west part. The map seems to be filled with a diffuse emission, which has no counterpart with the outer IR shell. Therefore, we conclude that it arises from the close H II region DR 15. In contrast, at 8 GHz, the array has resolved out most of the extended emission from the nebula, but the central object is still bright.

We have estimated the total flux density over the radio shell from our final images, with the one at 1.4 GHz having the best dynamical range and LAS, and that at 5 GHz being corrected for the flux loss. We have measured the flux densities using CASA. At 5 GHz, we also measured the background emission in different regions around the nebula and then we subtracted the average value from the total flux density. The flux density errors were determined as in

$$\sigma = \sqrt{(RMS_{\rm tot})^2 + (\sigma_{\rm cal} S_\nu)^2}. \quad (1)$$

Here, $RMS_{\rm tot}$ is the rms noise in the map integrated over the area covered by the source and $\sigma_{\rm cal}$ is the systematic relative error due to the flux calibrator (typically 3–5 per cent). For the 5-GHz measurements, $RMS_{\rm tot}$ was replaced with the standard deviation in the considered regions multiplied by the area of the source. The values found are $S(1.4\,{\rm GHz}) = 320 \pm 82$ and $S(5\,{\rm GHz}) = 323 \pm 126$ mJy. We highlight the fact that the 5-GHz error is large because of the background emission, which is non-uniform and makes our estimate uncertain. We also note that the 1.4-GHz value might be underestimated because it is not complemented with single-dish data. The values found are lower than those obtained by Higgs et al. (1994), who used interferometric and single-dish observations, but probably did not subtract the background. This leads to the discrepancy with our measurements. We have also compared our flux densities at both frequencies with those measured on the EVLA:D maps (with the best LAS) over the radio shell in order to verify their consistency. We have found a good agreement.

3.2 Spectral index

To better understand the nature of the radio nebula, we have created a spectral index map between the EVLA:D+C 1.4- and 5-GHz maps. We have chosen these maps because they have comparable LAS (see Table 1). Before calculating the spectral index, we have re-gridded the map at 5 GHz to the grid of 1.4 GHz. We have converted the maps (originally in unit of Jy beam^{-1}) to Jy pixel^{-1}, dividing by the number of pixels contained in the area of a beam (at the HPBW). Then, we deconvolved the maps from their initial beams and reconvolved with a final beam of 27 × 25 arcsec^2. This operation is equal to the convolution with a Gaussian beam with $\sigma^2 = (1/8ln2)(HPBW_{\rm i}^2 - HPBW_{\rm f}^2)$. Finally, the spectral index

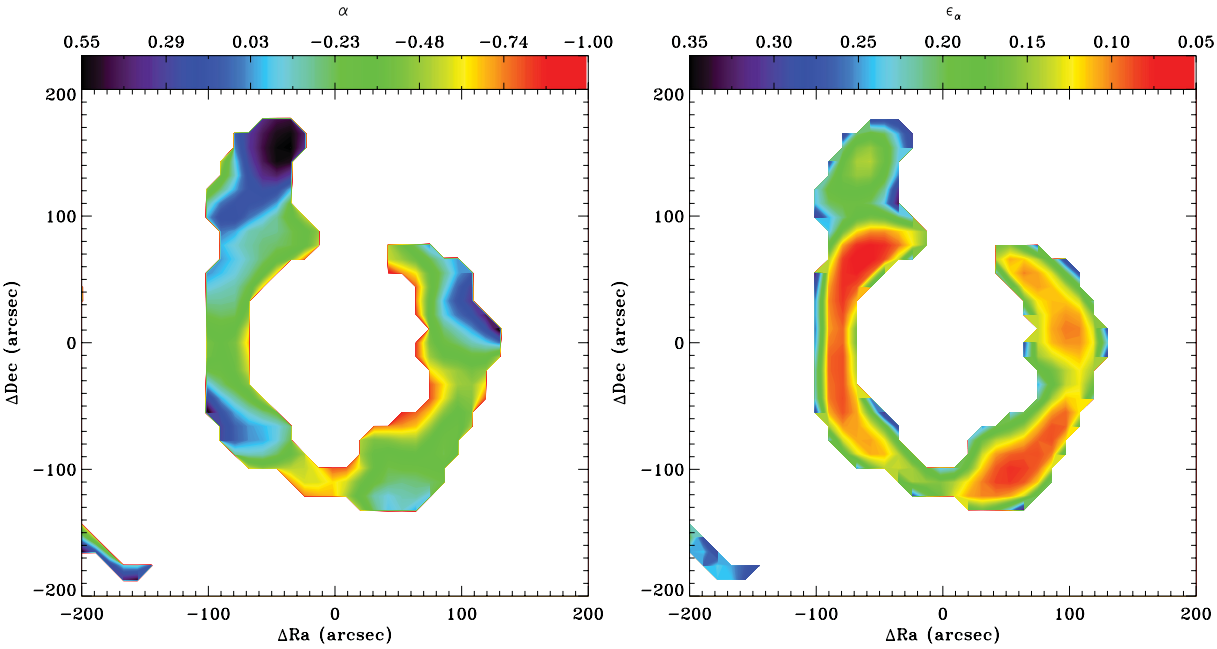

Figure 2. Left: spectral index map of G79 between 1.4 and 5 GHz. Right: error spectral index map.

map was calculated by discarding pixels below 5σ, where the noise was evaluated in the reconvolved images. Considering the error for the flux as in equation (1) (in units of Jy pixel^{-1}), with the uncertainty of the calibrator flux $\sigma_{\rm cal}$ equal to 3 per cent at 5 GHz and 5 per cent at 1.4 GHz, we have also estimated the error spectral index map. The spectral index and error maps are plotted in Fig. 2.

Over the nebula, the average spectral index $\langle\alpha_{\rm neb}\rangle$ is -0.29 ± 0.15, which is consistent with the theoretical value (-0.1) for optically thin H II regions emitting free–free radiation. The lower limit of $\langle\alpha_{\rm neb}\rangle$ is -0.44, indicating that the flux density at 5 GHz is underestimated because of flux loss resulting from the interferometer. The value of $\alpha_{\rm neb}$ varies slightly in some interesting regions. For example, in the south-west part of the nebula, close to the IR dark cloud (IRDC; Kraemer et al. 2010), $\alpha_{\rm neb} = -0.18 \pm 0.14$, which is still consistent with optically thin free–free but slightly higher than $\langle\alpha_{\rm neb}\rangle$. We can speculate that this is a modified region because of shock (Paper I). On the spur-region, the maximum value of $\alpha_{\rm neb}$ is 0.55, with an error of 0.17. This value is usually consistent with stellar winds, but in this case it is more likely because of emission from density clumps with a turn-over frequency between the considered frequencies. This spur-region is not correlated with the IR emission of G79.29+0.46 and, at the moment, we are not able to establish whether it belongs to the nebula or whether it is really a foreground/background emission region.

To derive the nature of the central source, we have determined its spectral index between 5 and 8 GHz from the corresponding flux densities. Therefore, we have measured its flux density by fitting a Gaussian around the source in both maps. As a result, we have found $S(4.96\,{\rm GHz}) = 1.81 \pm 0.08$ and $S(8.46\,{\rm GHz}) = 2.35 \pm 0.19$ mJy, where the error is determined as in equation (1). Therefore, we estimated the spectral index $\alpha_{\rm centre}$ by using these measurements. The spectral index error was obtained by adopting the error propagation for independent measures. We find $\alpha_{\rm centre} = 0.83 \pm 0.18$, which is consistent with a stellar wind ($\alpha = 0.6$). The measurements we are comparing come from observations at different epochs (2005 and 2010 for the 8- and 5-GHz data sets, respectively). However, although LBVs can suffer from changes in the mass-loss rate (e.g. AG Car; Stahl et al. 2001; Vink & de Koter 2002; Groh et al. 2009), G79.29+0.46 has not yet shown any important variability. Therefore, we are confident that the two data sets are compatible. Previously, through their observations of the central object at 4.86 and 8.46 GHz, Higgs et al. (1994) derived a spectral index of 1.39 ± 0.14, which is steeper than the canonical value. This is very likely because they obtained a larger beam at 8.46 GHz (∼11 arcsec) and therefore the flux measurement was contaminated by circumstellar or background emission. They pointed out that their spectral index is still consistent with mass loss from a stellar object. With our estimate, we can now confirm that the central object detected is a stellar wind from the cLBV G79.29+0.46.

3.3 Ionized mass

Once the nature of the radio nebula is known, we can estimate its average electron density and its ionized mass, because for a nebula of H, emitting free–free radiation and with a temperature about 10^4 K, the optical depth τ_ν can be expressed as

$$\tau_\nu = \int \kappa_\nu \, {\rm d}l = 8.24 \times 10^{-2} \left(\frac{T_{\rm e}}{\rm K}\right)^{-1.35} \left(\frac{\nu}{5\,{\rm GHz}}\right)^{-2.1} \frac{EM}{\rm pc\,cm^{-6}}. \quad (2)$$

Here, the emission measure (EM) is

$$EM = \int_0^s n_e^2 {\rm d}s \ ({\rm pc\,cm^{-6}}). \quad (3)$$

Therefore, we can use the optical depth map (as determined from the radiative transfer equation in the case of optically thin emission not absorbed along the line of sight and considering the Rayleigh–Jeans approximation for the Planckian, valid in the radio domain) to obtain the emission measure and hence the average electron density from the radio measurements. For this analysis, we refer to the final image at 5 GHz (Fig. 1), because it covers all the angular scales of the considered region.

Before calculating the optical depth, we have subtracted the background emission (estimated by averaging the values found in different regions on the map) and we have converted the map from

units of Jy beam^{-1} to Jy pixel^{-1}, as before. We find an average τ_ν of ∼0.2. Therefore, the average value for $\langle EM \rangle$ over the shell is 680 ± 270 pc cm^{-6}. The error in $\langle EM \rangle$ takes into account the uncertainty of the flux density measurement. In order to calculate the electron density as well, we need to establish the geometrical depth of the nebula. We assume the geometry of a hollow sphere with average inner and outer radii of $\langle R_{\rm in} \rangle = 80$ arcsec (which corresponds to 0.66 pc at a distance of 1.7 kpc) and $\langle R_{\rm out} \rangle = 110$ arcsec (0.9 pc), respectively. Therefore, we assume an average geometrical depth $\langle s \rangle$ of 0.67 pc, and we find an average electron density of ∼32 ± 20 cm^{-3}. Finally, the ionized mass is 1.51 ± 0.96 M$_\odot$ in the considered volume. Modelling the radio flux densities, Higgs et al. (1994) obtained a mass of 6.3 M$_\odot$ at a distance of 1.7 kpc. They assumed a larger volume for the shell (with inner and outer radii of 95 and 130 arcsec, respectively) and very likely did not subtract the background/foreground contribution from the nebula emission. Adopting the same values and the electron density (∼45 ± 36 cm^{-3}) derived from the map not background-subtracted, we find a mass of 3.5 ± 2.8 M$_\odot$, which is lower than the value provided by Higgs et al. (1994), but still consistent within the error.

3.4 Current mass loss and spectral type of the star

Because the emission from the central object is a result of stellar wind (as shown in Section 3.2), from the measured flux density we estimate the mass-loss rate of the star, following Panagia & Felli (1975):

$$\dot{M} = 6.7 \times 10^{-4} v_\infty S_\nu^{3/4} D^{3/2} (\nu \times g_{\rm ff})^{-1/2} \ ({\rm M}_\odot \ {\rm yr}^{-1}). \quad (4)$$

Here, $S_\nu = 1.51$ mJy is the observed radio flux density at 4.96 GHz, $v_\infty = 110$ km s^{-1} (Voors et al. 2000a) is the terminal velocity of the wind and $D = 1.7$ kpc (Jiménez-Esteban et al. 2010). The free–free Gaunt factor $g_{\rm ff}$ is approximated as in Leitherer & Robert (1991): for a gas with an electron temperature of $T_{\rm e} = 10\,000$ K at 4.96 GHz, $g_{\rm ff} = 5.08$. Therefore, we find that the star is losing mass at a rate of

$$(1.4 \pm 0.2) \times 10^{-6} \left(\frac{v_\infty}{110 \, {\rm km \, s^{-1}}} \right) \left(\frac{D}{1.7 \, {\rm kpc}} \right)^{3/2} f^{1/2} \, {\rm M}_\odot \ {\rm yr}^{-1},$$

where f is the filling factor.

Once we have evaluated the ionized mass in the nebula (as in Section 3.3), we can provide an estimate of the ionizing photon flux from the star $F_{\rm UV}$, as

$$F_{\rm UV} = \frac{M_{\rm ion} \langle n_{\rm e} \rangle \beta_2}{m_{p({\rm M}_\odot)}}, \quad (5)$$

an approximation valid for an ionization bounded nebula (as found in Paper I). Considering the standard values for the recombination coefficient β_2 and the proton mass $m_{p({\rm M}_\odot)}$, we find $\log F_{\rm UV} = 46.24$, which corresponds to a spectral type from B2 to B1 for a supergiant I (Panagia 1973). Voors et al. (2000a) proposed a mid-B supergiant after an analysis of the optical and NIR spectra of the central object. However, the value we have found must not be considered as the current spectral type of the star, because the recombination time of the gas is much longer (tens of thousands years) than the typical LBV variability cycles (decades). This implies that the radio emission from the shell is not sensitive to changes in the stellar parameters. The spectral type derived with this method must be considered an average value over ∼10^4 yr.

4 ANALYSIS OF THE INFRARED CONTINUUM EMISSION

4.1 Morphology of the infrared nebula from the *Herschel* images

The high-resolution *Spitzer* images have been already described in different works, where it has been pointed out that the morphology of the IR nebula consists of multiple shells, indicative of mass-loss episodes at different epochs. These previous works have shown that there are at least two populations of dust: the hot one emitting in the infrared array camera (IRAC) bands, and the warm one emitting in the MIPS bands. The hot dust (∼1500 K) is distributed in the inner ring (with a peak at about ±100 arcsec), mostly cospatial with the ionized gas (Kraemer et al. 2010; Paper I). The warm dust (∼90–350 K) emitting at longer wavelengths (>24 μm) is more extended in the inner ring than the hot dust (Kraemer et al. 2010) and presents a further component in the outer shell (peaked at about ±200 arcsec; Jiménez-Esteban et al. 2010; Kraemer et al. 2010; Paper I). A central object, on the position of the star, is detected up to 24 μm.

Fig. 3 is a three-colour image obtained by superimposing the *Herschel*/PACS images at 70 μm (in blue), 100 μm (green) and 160 μm (red). We set up the absolute flux scale of the *Herschel* images by using the standard calibration method developed by Bernard et al. (2010). The 70- and 100-μm images have a resolution comparable to that of the *Spitzer*/MIPS image at 24 μm, while at 160 μm it is comparable to that of the MIPS image at 70 μm (see Table 4 and Fig. 4). The 70- and 100-μm maps show the overall morphology of the 24-μm emission, probing the warm dust distributed in the inner and outer shells. However, we note that the broad inner shell reveals another component, peaked at about ±150 arcsec, leading to a total of three dusty shells (as indicated with arcs in Fig. 3). The first two shells (the wide bright one peaked at ±100 arcsec and the close faint one peaked at ±150 arcsec) also have a counterpart at 160 μm. At this wavelength, there are also hints of the outer shell, but the background is high and confusion becomes dominant. For the photometric measurements, in this case we concentrate only on the two inner shells (lower limit). We also note that the central object is quite bright at 70 and 100 μm and weaker, but still visible, at 160 μm.

In the SPIRE bands (250, 350 and 500 μm) the central object is not detected, the nebula is less bright, and the IRDC in the south appears in emission (as evident in the bottom panels of Fig. 4). At these wavelengths, there are hints of arcs in the position of the inner shell, but the IRDC becomes brighter and contaminates the shell emission. For this reason, in our analysis we refer only to the 70-, 100- and 160-μm images. The absence of further nebular features in the position of the nebula might exclude the presence of a cold dust component, even if it could be not detected because it is too faint relative to the surrounding interstellar medium.

4.2 Analysis of the infrared emission

We have measured the flux densities of the nebula around G79.29+0.46 by using the package SKYVIEW,[2] release 3.6. We remind the reader that all the images we have used are summarized in Table 4. Considering the circular shape of the nebula, flux densities were evaluated in circles enclosing the emitting regions to the specific wavelength (as indicated in Table 5).

[2] http://www.ipac.caltech.edu/skyview/

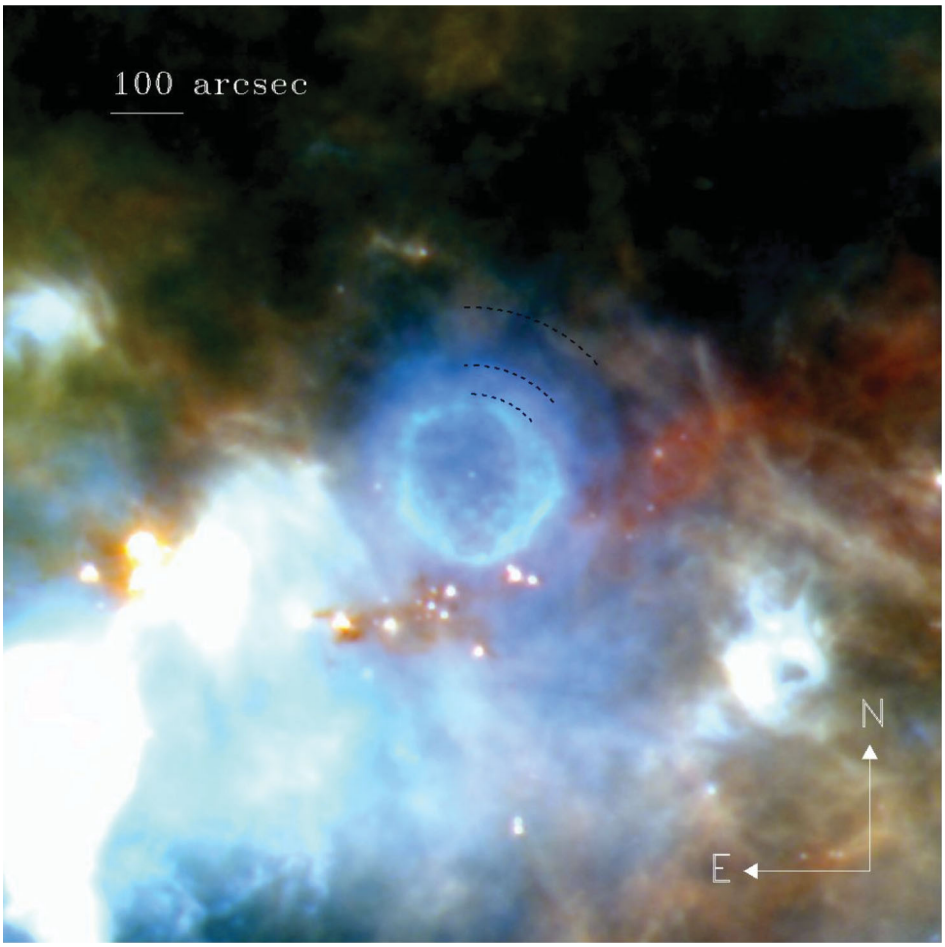

Figure 3. Three-colour image of the nebula around G79.29+0.46 from the *Herschel* data at 70 μm (blue), 100 μm (green) and 160 μm (red). The edges of the three shells are highlighted with arcs.

To take into account the strong diffuse emission around the nebula, we evaluated the background in annuli close to the nebula and we subtracted it from the integrated flux densities. As already mentioned, the background is important and extremely variable, especially at the longer wavelengths (≥24 μm), and this causes a high uncertainty in its determination (∼15–25 per cent). This uncertainty, integrated over the emission region, causes errors up to ∼50–70 per cent on the flux densities. In Table 5, we report flux densities and their errors at all wavelengths. Note that in the table, the flux density error includes only calibration uncertainties.

4.3 Nature of the infrared central object

Hot stars such as G79.29+0.46 are not expected to be detected at longer wavelengths. However, at the position of the star, the *Herschel* images show compact emission at 70, 100 and 160 μm. To understand the nature of this emission, we consulted the NASA/IPAC Infrared Science Archive (IRSA) point source catalogues and derived the NIR and mid-IR flux densities of the star from the Two-Micron All-Sky Survey (2MASS) *J*, *H*, *K* and *WISE* magnitudes.[3] We also included the IRAC and MIPS photometric measurements from the *Spitzer* Legacy Survey of the Cygnux-X complex (Hora et al. 2007). For flux densities at longer wavelengths (PACS bands), we used our own measurements, obtained by using an aperture of 6 arcsec and the following aperture correction: 1/(0.701,0.672,0.438) at 70, 100 and 160 μm, respectively. The mentioned flux densities for the central source are listed in Table 6.

Thus, we have fitted the IR photometric data with blackbody and greybody functions, following the method used by Flagey et al. (2011b) to constrain the nature of other hot stars surrounded by mid-IR shells by means of IRS spectra and NIR to mid-IR photometric measurements. In the fitting, we have also included the IRS/SL spectrum (Section 5) taken on the position of the star. We note that the photometric data match very well the IRS data without any scaling factor, despite the fact that the background is evaluated in different regions. We find that a minimum of five components are required to obtain a decent fit of the complete spectral energy distribution (SED). We impose in particular a blackbody for the central star and $\nu^2 B_\nu$ greybodies for the other components. We set the effective temperature of the star $T_{\rm eff} = 20\,000$ K. The free parameters are the four dust temperatures from T_1 to T_4, the amplitudes of the black/greybodies, and the extinction expressed as a depth $\tau_{9.7}$. Each of these parameters can vary within a defined range: $T_{\rm eff}$ from 20 000 to 24 000 K; T_1 from 500 to 2500 K; T_2 from 150 to 500 K; T_3 from 50 to 150 K; T_4 from 30 to 100 K; $\tau_{9.7}$ from 0 to 10. A best fit is shown in Fig. 5.

[3] The 2MASS and WISE magnitudes were transformed into flux densities using their well-known zero values (see their release notes).

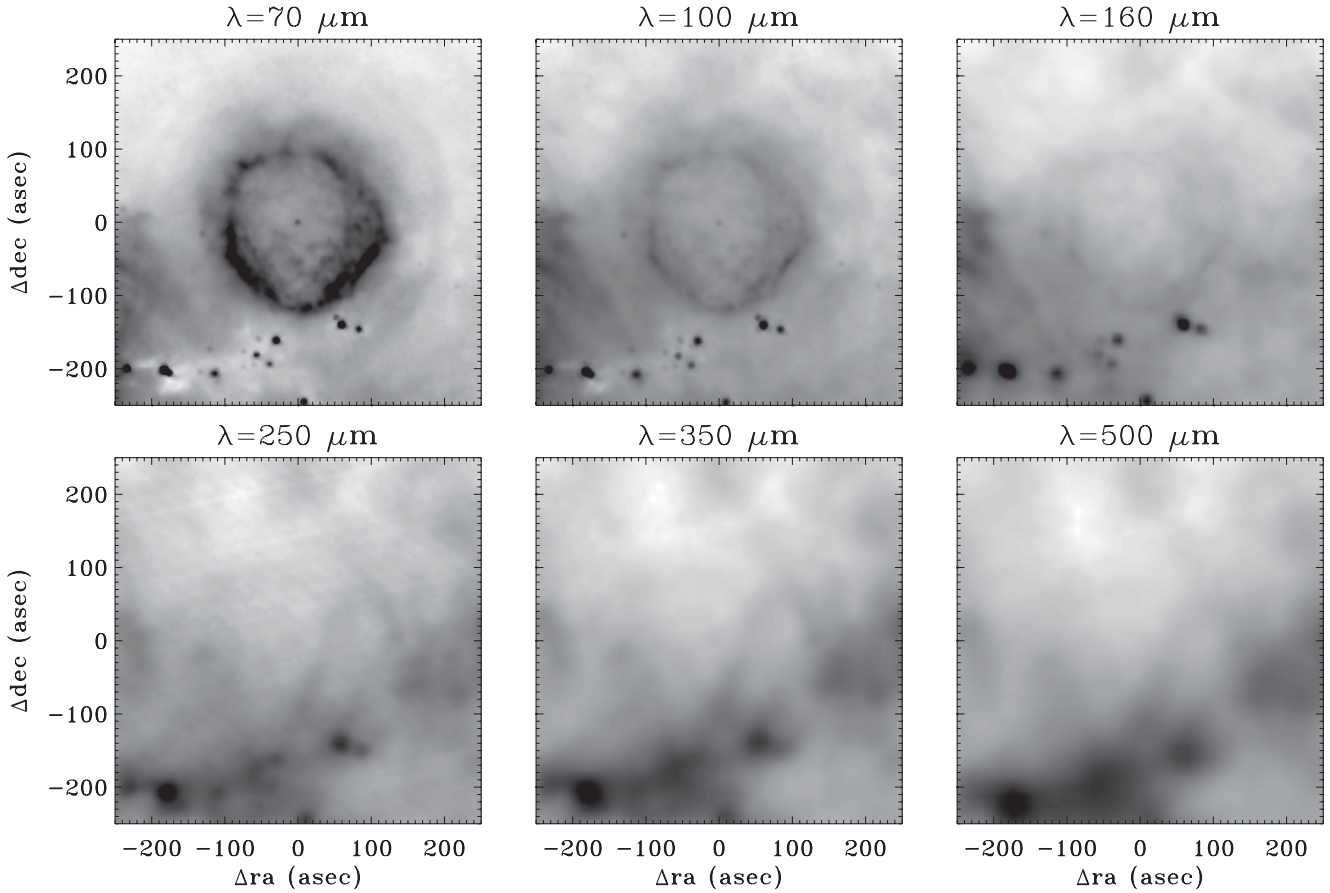

Figure 4. The *Herschel* images of G79.29+0.46. The upper plots show PACS 70 μm (left), 100 μm (centre) and 160 μm (right). The lower plots show SPIRE 250 μm (left), 350 μm (centre) and 500 μm (right). For each map, the field of view is about 4 × 4 arcmin^2 centred on the central source position.

Table 5. Total flux densities of the IR nebula.

λ (μm)	Total flux density (Jy)[a]	Instrument
8.69	7.74 ± 1.55[b]	ISOCAM01
11.48	11.94 ± 2.39[b]	ISOCAM01
12	14.8 ± 2.0[b]	*WISE*-W3
12.41	8.9 ± 1.8[b]	ISOCAM01
13.53	9.11 ± 1.82[b]	ISOCAM01
15.96	20.6 ± 4.1[c]	ISOCAM01
22	166.1 ± 17.0[d]	*WISE*-W4
24	165.8 ± 17.0[d]	MIPS
25	194.9 ± 20.0[d]	*IRAS*-HiRES
60	725.6 ± 218.0[d]	*IRAS*-HiRES
70	552.2 ± 110.0[d]	MIPS
70	583.7 ± 117.0[d]	PACS
100	500 ± 350[d]	PACS
160	31.8 ± 10.0[e]	PACS

[a]Errors include only calibration uncertainties.
[b]Inside a circle with a radius of 1.96 arcmin.
[c]Inside a circle with a radius of 2.2 arcmin.
[d]Inside a circle with a radius of 3.6 arcmin.
[e]Inside a circle with a radius of 3 arcmin.

Table 6. Total flux densities of the IR central object.

λ (μm)	Total flux density (Jy)[a]	Instrument	Comment
1.235	2.73 ± 0.02	2MASS	2MASS Catalogue
1.662	7.81 ± 0.04	2MASS	2MASS Catalogue
2.159	12.37 ± 0.04	2MASS	2MASS Catalogue
3.4	10.17 ± 4.51	W1	*WISE* Catalogue
3.6	10.57 ± 1.05	IRAC	Cyg-X Legacy Catalogue
4.5	9.40 ± 1.00	IRAC	Cyg-X Legacy Catalogue
5.8	6.82 ± 0.50	IRAC	Cyg-X Legacy Catalogue
8.0	4.60 ± 0.40	IRAC	Cyg-X Legacy Catalogue
12.0	2.32 ± 0.05	W3	*WISE* Catalogue
22.00	0.93 ± 0.04	W4	*WISE* Catalogue
23.99	1.08 ± 0.02	MIPS	Cyg-X Legacy Catalogue
24.0	1.01 ± 0.05	MIPS	This work
70.0	0.44 ± 0.04[a]	PACS	This work
100.0	0.30 ± 0.03[a]	PACS	This work
160.0	0.11 ± 0.03[a]	PACS	This work

[a]Errors include only calibration uncertainties.

The derived parameters are the temperatures (≃1170, 340, 145 and 40 K) of the four dust components, the depth at 9.7 μm (1) and the reduced χ^2 (46.87). However, we draw attention to the fact that, because of the many degrees of freedom and the possible degeneracy between them, we find many similar best fits with slightly different final parameters, depending on the initial guess of the fit. The four dust component temperatures should thus be seen as rough estimates. We suggest that there is a range of temperatures, well described by the range explored by T_1 to T_4, in a circumstellar envelope close to the central star. The temperature of the star is

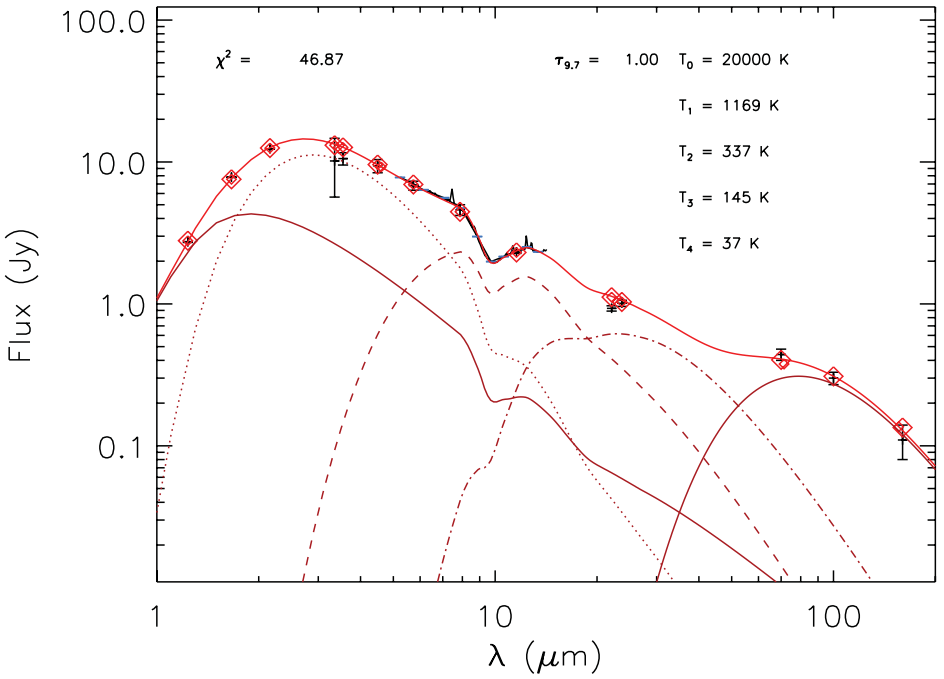

Figure 5. Five-component fitting of the central source SED. Red diamonds are the best-fitting values and show both the star (blackbody) and four dust components ($\nu^2 B_\nu(T)$ greybodies). Black crosses are the observed values. The IRS/SL spectrum is shown in blue. The derived parameters are given: temperature T_i for each component, the reduced χ^2 and the optical depth at 9.7 μm.

not well constrained, as shown in the figure, because the blackbody contributes very little to the *J* band only.

The IRS spectrum[4] (described in Section 5) gives strong evidence that an absorption feature is present at 10 μm because of astronomical silicates. Therefore, we use the depth $\tau_{9.7}$, as obtained in the fit, to determine the visual extinction A_V towards the star, by means of the extinction curve determined by Mathis (1990). We find $\tau_{9.7} = 1$ (with an uncertainty of about 10 per cent). Therefore, we obtain $A_V = 18.6$ in the case of a constant total-to-selective parameter $R_V = 3.1$ (a typical value for small grains in the Milky Way).

Visual extinction of G79.29+0.46 has been determined by various authors and optical/NIR observations of the source have provided diverse values for A_V. For example, Higgs et al. (1994) found a value of 16 ± 1 mag, by comparing the shape of the observed red continuum with the reddened model continua of early-type stars. Trams et al. (1999) derived $A_V = 11.9$ mag by studying the IR properties of G79.29+0.46. Voors et al. (2000a) derived a visual extinction of 14.9 mag by means of *JHK* spectra, assuming an effective temperature of 18 000 K and the extinction law by Torres-Dodgen, Carroll & Tapia (1991). Voors et al. (2000a) also measured the extinction from the diffuse interstellar bands (DIBs), by using a relation between the strengths of these bands and $E(B-V)$, valid in several OB associations in Cygnus. In this case, they found $A_V \sim 6.4$ mag, which is much less than the value derived previously. As a reason for the discrepancy between the two methods, they explained that the DIBs do not measure the extinction due to molecular clouds, while G79.29+0.46 is very close to the obscured star-forming region DR 15. Because of the many degrees of freedom of our model, we can not assess which method among these is the best for determining the extinction towards the star. For the moment, we assume that A_V must range between ∼6 and ∼18.6 mag (see Section 5.1 for more details about extinction).

[4] For this analysis, we do not apply extinction correction.

4.4 Infrared physical properties of the extended nebula

Following a simple method described by Dayal et al. (1998) and Umana et al. (2010), we have also estimated the dust temperature and mass for the dust components in the extended nebula. The average dust temperature can be derived by interpolating a Planckian distribution between two observed brightnesses. Assuming that the IR continuum emission observed is due to thermal dust[5] and is not absorbed by colder dust along the line of sight. From the radiative transfer equation and the optical depth, we can derive the column density, ρl and, therefore, the mass of the nebula as

$$M = \rho l \Omega D^2. \quad (6)$$

Here, ΩD^2 is the physical area covered by the emitting region. For the analysis of the hot dust, we consider the ISOCAM maps at 8.69 and 13.53 μm, which have the same resolution. In this analysis, we do not consider the IRAC maps because they are too contaminated by the saturated star emission. From the measured ISOCAM flux densities in Table 5, we have subtracted the stellar component, through aperture photometry. After this subtraction, we estimated for the nebula the following flux densities: $S(8.69\,\mu\text{m}) = 6.5 \pm 1.3$ and $S(13.53\,\mu\text{m}) = 8.3 \pm 1.7$ Jy. For the analysis of the warm dust component, we refer to the *Spitzer*/MIPS 24-μm and the *Herschel*/PACS 70-μm maps, given their similarity in resolution. The nebula flux densities in this case are $S(24\,\mu\text{m}) = 165 \pm 17$ and

[5] Our spectroscopic analysis in Section 5 shows that there is no evidence for the presence of polycyclic aromatic hydrocarbons (PAHs). However, emission lines can contaminate the continuum emission at wavelengths <15 μm.

Table 7. Assumed chemical composition, grain size and absorption coefficient. We also show the derived optical depth, temperature and mass of the dust, where λ_1 and λ_2 are 8.69 and 13.5 μm, respectively (for hot dust) and 24 and 70 μm (for warm dust).

Composition and size (μm)	κ_{λ_1} (cm^2 g^{-1})	κ_{λ_2} (cm^2 g^{-1})	τ_{λ_1}	τ_{λ_2}	T (K)	M_{λ_1} ($M_\odot$)	M_{λ_2} ($M_\odot$)
Hot dust							
Silic. (0.01, 0.1)	762	743	$(2.5 \pm 0.5) \times 10^{-9}$	$(3.5 \pm 0.7) \times 10^{-9}$	518 ± 210	$(4.6 \pm 0.9) \times 10^{-8}$	$(6.5 \pm 1.3) \times 10^{-8}$
Silic. (1)	807	920	$(1.7 \pm 0.3) \times 10^{-9}$	$(2.6 \pm 0.5) \times 10^{-9}$	587 ± 238	$(2.9 \pm 0.6) \times 10^{-8}$	$(4.0 \pm 0.8) \times 10^{-8}$
Graph. (0.01)	390	230	$(1.1 \pm 0.2) \times 10^{-8}$	$(9.5 \pm 2.0) \times 10^{-9}$	357 ± 145	$(3.9 \pm 0.8) \times 10^{-7}$	$(5.8 \pm 1.2) \times 10^{-7}$
Graph. (0.1)	476	257	$(1.4 \pm 0.3) \times 10^{-8}$	$(1.1 \pm 0.2) \times 10^{-8}$	336 ± 136	$(4.2 \pm 0.8) \times 10^{-7}$	$(6.3 \pm 1.3) \times 10^{-7}$
Graph. (1)	1980	985	$(1.9 \pm 0.4) \times 10^{-8}$	$(1.4 \pm 0.3) \times 10^{-8}$	319 ± 129	$(1.30 \pm 0.3) \times 10^{-7}$	$(2.0 \pm 0.4) \times 10^{-7}$
Warm dust							
Silic. (0.01, 0.1, 1)	647.7	69	$(4.0 \pm 0.4) \times 10^{-4}$	$(4.2 \pm 0.8) \times 10^{-5}$	59 ± 18	0.032 ± 0.006	0.032 ± 0.006
Graph. (0.01)	300	107	$(6.1 \pm 0.6) \times 10^{-5}$	$(2.2 \pm 0.4) \times 10^{-5}$	72 ± 22	0.011 ± 0.002	0.011 ± 0.002
Graph. (0.1)	309	109	$(6.2 \pm 0.6) \times 10^{-5}$	$(2.2 \pm 0.4) \times 10^{-6}$	72 ± 22	0.010 ± 0.002	0.010 ± 0.002
Graph. (1)	600	300	$(3.6 \pm 0.4) \times 10^{-5}$	$(1.8 \pm 0.4) \times 10^{-5}$	77 ± 23	0.0031 ± 0.006	0.0031 ± 0.006

$S(70\,\mu\text{m}) = 583 \pm 117$ Jy after subtraction of the central source contribution.

For hot grains, with an average temperature of ∼552 K (silicate) or ∼337 K (graphite), the resulting average mass is very small (∼10^{-7} $M_\odot$) and hence negligible. The warm dust has an average temperature of 59 K (graphite) or 74 K (silicate) and is more massive (3.2×10^{-2} or 8.0×10^{-3} $M_\odot$, for graphite or silicate, respectively). In all cases, the dust is optically thin. The temperature and mass are summarized in Table 7, as derived for both the hot and warm dust components. Note that they depend on the chemical composition and are obtained by assuming single grain sizes, as indicated. Uncertainties take into account only the flux density errors. By using a dust model to fit the *IRAS* images, Waters et al. (1996) provided a lower limit for the inner shell temperature of about 65 K. They also derived a dust mass of 0.14 $M_\odot$. To understand the discrepancy with our dust mass (a few 10^{-2} $M_\odot$), we have used the model described by Waters et al. (1996) and Izumiura et al. (1997), based basically on the integration of the mass-loss rate. By using our parameters, we find good agreement between the two methods. Therefore, the discrepancy is mostly a result of the assumed parameters, in particular the mass-loss rate and the outer radius of the shell, very likely overestimated in Waters et al. (1996) because of the bad resolution of the *IRAS* images. Modelling the 8- and 24-μm emission from the *Spitzer*/MIPS image with a radiative transfer code, Kraemer et al. (2010) found slightly higher temperatures (87–108 K), in the hypothesis of a carbon-rich nebula with amorphous carbon grains, but they considered a larger distance for G79.29+0.46 in their calculations ($D = 3$ kpc).

A mixed composition of silicate and graphite in dust has been observed in LBVNe (e.g. Wray 17-96; Egan et al. 2002). Similarly, we assume that the nebula around G79.29+0.46 has a mixed chemistry and, considering the average masses for silicate and graphite, we derive an average total dust mass of 0.02 $M_\odot$. This leads to a gas-to-dust ratio of ∼80, with the ionized mass of 1.51 $M_\odot$ (as estimated in Section 3.3). The value found is lower than the galactic interstellar case (100), but is still consistent. However, this must be considered a lower limit, because we are not taking into account the neutral mass very likely distributed in the outer shell.

5 ANALYSIS OF THE MID-INFRARED SPECTRA

In this section, we present our analysis of the archival mid-IR and FIR spectra collected by the LWS and SWS on board *ISO* and by the instrument IRS on board *Spitzer*. The positions of the spectrometers during the *ISO* and *Spitzer* observations are shown in the Appendix (see Figs A1 and A2). For the IRS spectra, we refer to the data obtained after the background subtraction. Data taken at the same channel were also merged in order to work with a spectrum per module. The mentioned spectra are shown in the Appendix (see Figs A3–A5). Because G79.29+0.46 is a heavily reddened object, before analysing the observed lines, the fluxes must be corrected for extinction along the line of sight. For the analysis, we refer only to the corrected fluxes.

5.1 Correction for extinction

Recent studies on the Cygnus-X region report median values for A_V of 5.6 (Hanson 2003) and 5.7 (Albacete Colombo et al. 2007), respectively, based on NIR and X-ray observations. To correct the IR spectra for interstellar extinction, we have assumed that the visual extinction for the nebula must be similar to that determined from other stars in the same region. These values are much lower than that obtained by fitting the IR emission of the central source (Section 4.2). However, because we cannot estimate the intrinsic extinction of the source due to the shell and the dusty central object, we consider for the correction the lowest value of 5.6, keeping in mind that the derived line fluxes might be lower limits. However, in the analysis, we discuss the effects of taking $A_V = 18.6$ (Section 5.3). Therefore, we used $A_V = 5.6$ and the extinction law determined by Mathis (1990) for a constant total-to-selective parameter $R_V = 3.1$.

We measured line fluxes before and after the extinction correction. To derive the fluxes, we used the ISAP package version 2.1 and fitted the lines by means of single Gaussians, after having estimated the baseline, usually of the first order but in some cases of the second or third order. We report intensities with a signal-to-noise ratio (S/N) usually larger than 5. The errors are the result of uncertainties in the background fitting procedure and do not take into account the absolute calibration errors (better than 5 per cent for IRS and SWS, and than 7 per cent for LWS). An additional uncertainty component, not included because it is unknown, arises from the extinction curve. Line fluxes are listed in the Appendix (Tables A1–A5).

5.2 Detected lines and shock-versus-photodissociation region diagnostics

The mid-IR and FIR spectra of G79.29+0.46 are rich in ionic and atomic fine-structure lines (e.g. [C II], [O I], [Si II], [Fe II]), similarly to other LBVs (e.g. HR Car; Umana et al. 2009). In G79.29+0.46,

this was first pointed out by Wendker et al. (1998) and Jiménez-Esteban et al. (2010). However, after the background subtraction from the IRS spectra, we find some differences with Jiménez-Esteban et al. (2010). For instance, some emission lines disappear. In particular, the [F I] 24.75-μm and [Si II] 34.80-μm lines. [Ar II] (or [Ne II]) 6.97-μm, [Ar III] 8.99-μm, [Ar III] 21.82-μm, [Ne III] 10.88-μm and [Ni II] 10.68-μm are also not present.[6] [Ni II] 10.68-μm is visible, but it does not reach 3σ. We also do not detect the H_2 transitions at 17.03 and 28.21 μm. All these lines surely arise from the interstellar medium.

Jiménez-Esteban et al. (2010) attributed emission lines in the band of the unidentified infrared (UIR) features (centred at 3.3, 6.2, 7.7, 8.6 and 11.3 μm) to PAHs. After subtracting the background emission, we find that these features in the IRS/SL disappear. Therefore, the emission in the UIR bands observed by Jiménez-Esteban et al. (2010) is interstellar. In the Appendix, Fig. A1 gives an indication that the mentioned lines belong to the interstellar medium. Conversely, the lines shown in Fig. A5 arise from the nebula (as shown in Fig. A1). According to Jiménez-Esteban et al. (2010), we confirm the absence of [S I] 25.2-μm.

The *ISO*/LWS spectra have strong [O I] 63-μm, [O III] 52- and 88-μm, [N II] 122-μm and [C II] 157-μm line emissions (we remind the reader that unfortunately *ISO* off-nebula observations are not available in the archives). The [N II] 122-μm line is indicative of high-ionization regions. Together with the [O III] 88-μm line, it is brighter inside the inner shell, along the east–west direction. The presence of both transitions in the outer shell also indicates an extended nature of the ionized gas. We cannot exclude that it is interstellar diffuse gas, because off-nebula observations are not available. However, the line fluxes vary across the nebula, and hence at least some of it might belong to the source.

Looking at the [O I] 63.2-μm line fluxes detected with *ISO*/LWS, we can see that they are very similar in flux over the nebula. The [O I] emission is typical of shocked regions or of photodissociation regions (PDRs). This line is the main cooling transition in the dense post-shocked region of dissociative shocks (Giannini, Nisini & Lorenzetti 2001; van Loon et al. 2010). When the [O I] line is fainter than the [O III] line, it indicates the absence of strong interactions (van Loon et al. 2010). In this case, the [O I] line forms in PDRs, while [O III] is typically strong in high-ionized diffuse gas (Mizutani, Onaka & Shibai 2002). The comparison in the LWS spectra between these two transitions seems to exclude the presence of shocked regions, but background observations are needed in order to be sure that all the line emission arises from the nebula. Another indicator of shocked regions or PDRs is the line pair [O I] 63-μm/[C II] 157.7-μm (Tielens & Hollenbach 1985). Strong [C II] emission is typical of PDRs. In particular, when the ratio is less than 10, then the presence of a PDR is favoured. From the analysis of this ratio in our LWS, it seems to exclude the presence of shocked regions in the area covered by the observations (Fig. A2). It is clearly evident that a PDR is present between the H II region, probed by free–free emission, and the molecular cloud, probed by rotational CO line emission (Rizzo et al. 2008). However, because we do not have background data sets for these spectra, we cannot exclude the fact that this gas belongs to the diffuse interstellar medium. For this reason, we neglect the PDR mass in the total nebula mass estimation.

[6] However, these lines detected by Jiménez-Esteban et al. (2010) might be present in other IRS data sets, which we have not re-analysed because off-nebula observations were not available.

[O III] 51.8-μm is particularly bright in the north-east part of the second shell, next to the radio spur-emission (see Fig. 1). Analysis of the radio spectral index in this region has shown us a value (0.55) different from optically thin free–free emission. Excluding excitation by a shock, this higher [O III] emission in the nebula outskirts might be attributed to density clumps.

5.3 Electron density from mid-infrared line ratios

The mid-IR lines of [S III] can be used for electron density diagnostics in a nebula. In fact, Houck et al. (1984), Moorwood et al. (1980) and Mizutani et al. (2002), and later Smith et al. (2009), computed the [S III] 18.7-μm/[S III] 33.5-μm line ratio dependence on the electron density. They found that this ratio, temperature-independent, is sensitive to change on the electron density in the range $100 \leq n_e \leq 10^4$ cm^{-3}. Hence, we have derived the [S III] 18.7-μm and 33.5-μm line fluxes present in the *ISO* SWS spectrum, positioned approximately on the nebula centre (Fig. A2). We remind the reader that in this case background observations are also not available. The two transitions have measured and dereddened fluxes, as in Table A1. Interstellar absorption is still important at 18 μm and for this reason we consider the dereddened values.

The derived line ratio is $F(18.7\ \mu\text{m})/F(33.5\ \mu\text{m}) = 0.74 \pm 0.47$, which corresponds to an electron density of ∼250 cm^{-3}. The error in this ratio is because of the uncertainty in the measured lines and is derived using the error propagation for independent measures. Similarly, by using the same line pair present in the IRS spectra on the central source (in particular, the line at 33.5 μm from the LH spectrum and the line at 18.7 μm from the SH spectrum), we found a ratio of 1.45, which corresponds to a density of $\sim 10^3$ cm^{-3}. We took into account the difference in areas covered by the LH and SH modules (11.1×22.3 and 4.7×11.3 arcsec^2, respectively), rescaling the flux at 33.5 μm by an approximated factor of $(4.66)^{-1}$.

We note that the electron density estimate from the IRS line pair is an order of magnitude higher than the values found from the SWS lines. This might be because the SWS spectra are not background-subtracted and it might also be because of the larger area of the SWS slit with respect to the IRS modules: as a consequence, the central value is averaged with smaller densities far from the centre. Our estimate is also larger than that of Jiménez-Esteban et al. (2010), who found an electron density of ∼500 cm^{-3}. The reason for this could be the fact that they did not correct for extinction, which is still important at 18.7 μm.

The [O III] 88.4-μm/51.8-μm line pair is a more sensitive indicator of the electron density, with respect to the [S III] 33.5-μm/[S III] 18.7-μm line pair (Houck et al. 1984). Using the LWS spectra, we have determined [O III] 88.4-μm/51.8-μm line ratios at six different positions on the nebula.

The derived line ratios and electron density estimates are listed in Table 8. Only in two cases is the ratio just below the low-density limit of 0.57 (Mizutani et al. 2002), and therefore, we provide an upper limit for the electron density. The low electron density region coincides with the inner shell (the high-ionized gas, observed also in the radio domain). We want to highlight the fact that electron densities estimated with this method must be considered to be upper limits, because the *ISO* spectra were not background-subtracted. However, these electron densities are still consistent with the mean value (32 cm^{-3}) found from the radio map (which probes the inner shell); however, this strongly depends on the geometry assumed (Section 3.3). We notice that at the stellar position, the electron density is higher ∼1000 cm^{-3} (from the IRS line ratio) and decreases to between ∼250 and ∼100 cm^{-3} next to the inner and

Table 8. Line ratios and electron densities.

Slit	Size (arcsec)^2	Relative position[a] (arcsec)^2	Line pair	Line ratio	n_e (cm^{-3})
IRS-SH/LH	4.7 × 11.3	0	18.5 μm/33.4 μm	1.45	∼1000
SWS-901	33 × 20	0	18.5 μm/33.4 μm	0.74	∼250
LWS-003	84 × 84	0	51.8 μm/88.4 μm	0.73	150–160
LWS-008	84 × 84	100 W	51.8 μm/88.4 μm	0.55	<100
LWS-014	84 × 84	100 E	51.8 μm/88.4 μm	0.53	<100
LWS-011	84 × 84	200 W	51.8 μm/88.4 μm	0.67	∼100
LWS-005	84 × 84	200 E	51.8 μm/88.4 μm	1.24	200–300
LWS-007	84 × 84	200 N-E	51.8 μm/88.4 μm	1.15	∼200

[a] With respect to the star's position.

outer shells, except in the north-east part of the second shell, where it increases again to ∼200 cm^{-3}. In fact, in this region, the [O III] line is particularly bright, as discussed in Section 5.2. This strengthens the indication of high-density (n_e > 100 cm^{-3}) clumps in the vicinity of G79.29+0.46.

Another pair of lines useful for a diagnostic study is the [Si II] 34.8 μm to [S III] 33.5 μm line, which indicates changes in the excitation due to distance from the star (Simpson et al. 2007), but for these lines our SWS data set covers only the central position on the nebula. However, the resulting ratio is ∼0.21, which is lower than the diffuse interstellar gas value (∼2.5) and instead is a typical value in the H II region (Simpson et al. 2007; Jiménez-Esteban et al. 2010). We note that [Si II] emission is absent in the background-subtracted spectrum from the IRS taken along the nebula.

We point out that this diagnostics is limited not only by the fact that the *ISO* spectra are not background-subtracted, but also by the uncertainty of A_V. However, we can exclude much higher values for A_V (such as the value determined from the IR central object, i.e. 18.6) than 5.6; in fact, we have found that $A_V = 18.6$ leads to electron densities (from the mid-IR lines) of the order of ∼10^5 cm^{-3}, not expected in LBV nebulae. In contrast, the values found in the spectroscopic analysis give an indication that the visual extinction for the nebula cannot be more diverse than the assumed value of 5.6.

6 MODELLING THE NEBULA WITH CLOUDY

Based on the physical parameters derived in our analysis, we have modelled the nebula around G79.29+0.49 with the photoionization code CLOUDY version c10.01, last described by Ferland et al. (1998). Almost all the assumptions for the model are derived from the observations and this has allowed us to adopt a simple method for the computation of the SED.

The first assumption is that the radiation that illuminates the nebula arises from a blackbody with a temperature between 18 500 and 20 400 K (consistent with a spectral type B2–B1, as derived in Section 3.4). The distance adopted is 1.7 kpc. The geometry for the nebula is spherical: based on the radio observations, it is a shell with an inner radius of 0.66 pc. A single shell is assumed. The density is constant within the Strömgren radius and then decreases with a law $\propto r^{-3}$. Abundances are chosen as solar. Dust grains are assumed to be composed of both graphite and silicate and are described by a power-law distribution (Mathis, Rumpl & Nordsieck 1977). By default, the grains are resolved into 10 size bins. The filling factor is assumed as unity. Cosmic rays are included.

The free parameters are the stellar luminosity, which has to range between about 10^5 and 10$^{6.3}$ L$_\odot$ (consistent with typical values for LBVs), the grain abundance and the blackbody temperature (in the range mentioned above). Therefore, we computed several grids of models and stopped each computation once a nebular mass of 1.53 M$_\odot$ was reached (according to our estimation). Keeping in mind the allowed range for the physical parameters as estimated in this work, we changed them, proceeding by iteration in order to explain the observations. In particular, first we set the blackbody to 20 000 K and varied the hydrogen density (approximated to the electron density, which could range between ∼30 and 200 cm^{-3}, according to our diagnostics). Starting from the lowest electron density, the first value that fits the radio flux density is then set (in fact, the dust emission was found to be weakly dependent on the assumed density with respect to the radio). Therefore, we varied the grain abundances and the stellar luminosity in order to fit the FIR and mid-IR observations, respectively. Finally, we adjusted the blackbody temperature and the hydrogen density in order also to obtain the best model for the mid-IR spectra.

The final model is shown in Fig. 6. The measured flux densities are overlaid. The input and output parameters of the CLOUDY model are listed in Table 9. As shown in the figure, the model is satisfactory at the longest wavelengths (e.g. radio and FIR). Note that at 160 μm we provided a lower limit for the flux density (Section 4.2). Conversely, the continuum mid-IR (<15 μm) does not describe the data. This can be explained in two ways. In the model, small grains are absent because they are destroyed by the radiation field. In reality, they survive because they are shielded by density clumps (as shown in the maps, the mid-IR emission is clumpy). In support of this, there is plenty of observational evidence that very small grains (VSGs) survive within H II regions (Flagey et al. 2011a; Paradis et al. 2011; Paladini et al. 2012) despite theoretical models predicting depletion or partial destruction of the grains. Recently, the mid-IR emission of LBV WRA 751 has also been explained as being a result of grains not in thermal equilibrium (e.g. Voors et al. 2000b; Vamvatira-Nakou et al. 2013). Otherwise, and this is more likely, there is a lack of hot dust and the observed photometric flux densities are mostly a result of the mid-IR lines at wavelengths <15 μm, as predicted by the CLOUDY model. Moreover, the IR continuum in the IRS spectra (Fig. A5) is very small, even at the longer wavelengths, suggesting that the observed photometric emission comes from line transitions. The gas-to-dust ratio in the model is ∼100, which is still consistent with the value found in Section 4.2.

We have also compared the predicted line ratios with those observed. The considered [O III] lines are collisionally excited and are sensitive to density. The average observed [O III] 51.80-μm/[O III] 88.33-μm ratio (0.81) is well predicted by the model (0.91). The [Fe II] 25.98-μm/[S III] 33.47-μm is found to be 0.02 in the model, two orders of magnitude smaller than the observed value of 0.3.

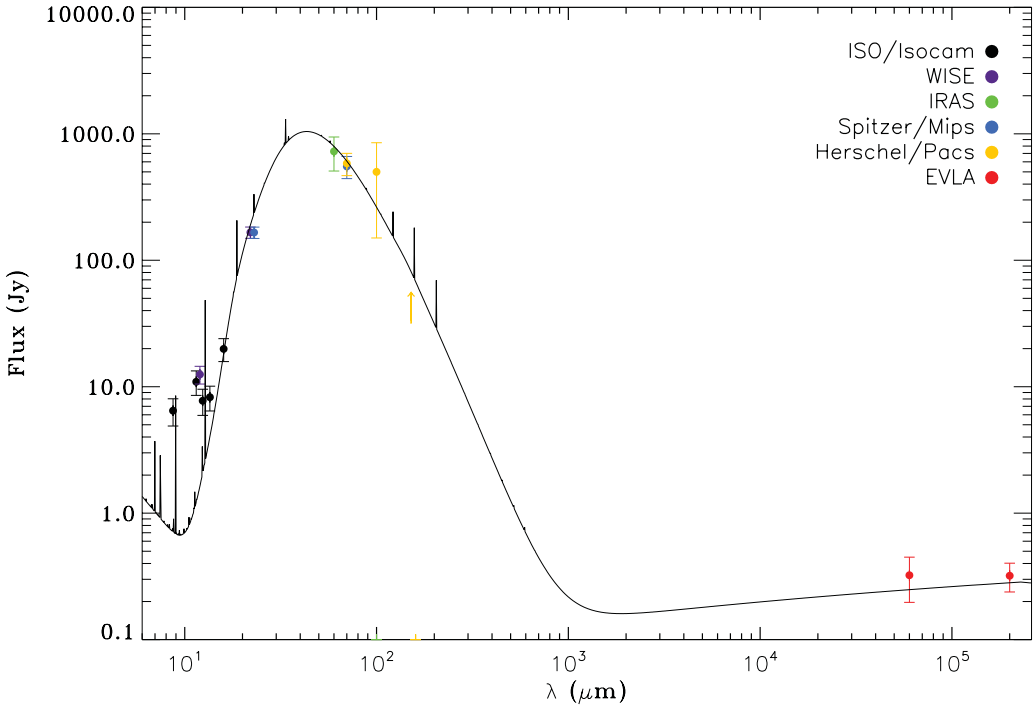

Figure 6. Model of the SED and observed flux densities of G79.29+0.46 from *Spitzer*, *ISO*, *WISE*, *IRAS*, *Herschel* and EVLA observations.

Table 9. Model parameters.

Parameter	Value
$T_{\rm eff}$ (K)	20 400
D (pc)	1700
$\log(r_{\rm in})$ (cm)	18.3085
$\log(r_{\rm in})$ (pc)	0.66
M ($M_\odot$)	1.53
$\log[L/(L_\odot)]$	5.4
$\log(n_{\rm H})$ (cm^{-3})	2.13
$T_{\rm e}$ (K)	5800
Gas/dust	99

To understand this discrepancy, we have obtained a grid of models by varying the blackbody temperature and we have found that the [Fe II] line is controlled by the ionization field and not by abundances. The [Fe II] 25.98-μm line is very common in PDRs, and therefore we suspect that it arises from a layer further out than the ionized gas. Another interesting finding is that the ratio of [Ne II] 12.81-μm/[Ne III] 15.55-μm observed in the centre of the nebula is 2.2, while the model predicts a higher ratio (∼700), because the photons are not sufficiently energetic to cause [Ne III] transitions. This strongly suggests that the presence of collisional excitation produces both the [Ne II] and [Ne III] transitions.

Line emission of [O I] 63.18 μm is not predicted by the model. Therefore, the observed lines in the LWS spectra are very probably of interstellar origin.

As a result of the model, the average electron temperature is 5800 K. The main heating process is photoelectric and the temperature of graphite grains over radius varies from 90 K (at the inner radius) to 57 K (at the outer radius), while for silicate grains it varies from 73 to 53 K. These values are consistent with our average estimates from the FIR images (see Table 7).

Finally, the derived stellar luminosity, $\log(L/L\odot) = 5.4$, is consistent with the value provided by different authors (from 5 to 6; e.g. Waters et al. 1996; Voors et al. 2000a) and with that of galactic LBVs (Humphreys & Davidson 1994).

The proposed model is based on the assumption that the nebula is a single shell, while the morphology clearly shows that it consists of multiple shells. However, because the bulk of the determined mass is distributed within the inner shell (at least 98 per cent), this simplifying assumption does not affect the model results. To verify this, we have also modelled multiple shells, by considering first the mass contained in the inner shell and giving the transmitted continuum in output as the incident radiation field for the second shell. We have found good agreement with the simple model.

The neutral mass, probably distributed in the outer shell, has not been taken into account in the total mass computation. Considering this, the total mass could be higher, as well as the gas-to-dust ratio. A similar model, with the same luminosity and effective temperature for the star, can still explain the observations up to a mass of 5 $M_\odot$ with proper adjustment of the gas-to-dust ratio.

7 DISCUSSION AND CONCLUSIONS

We have proposed a multiwavelength analysis of the nebula around the cLBV G79.29+0.46 by considering data in a wide spectral range (from the radio to the mid-IR). The aim of this work was to explain all the observed properties under the same hypothesis and to provide a comprehensive picture of the nebular properties.

We can summarize our findings as follows.

(i) Radio observations and the model obtained with the code CLOUDY have allowed us to constrain the physical parameters of the star, which has a luminosity of $\sim 10^{5.4}$ $L_\odot$ and an effective temperature of 20.4×10^3 K.

(ii) The star is currently losing mass through stellar winds (as found by an analysis of the central object spectral index) with a rate of

$$1.4 \times 10^{-6} \left(\frac{v_\infty}{110\,\mathrm{km\,s^{-1}}}\right) \left(\frac{D}{1.7\,\mathrm{kpc}}\right)^{3/2} f^{1/2}\,\mathrm{M_\odot\,yr^{-1}}.$$

(iii) An analysis of the IR emission of the central object reveals that the star is surrounded by a close dusty envelope with a temperature in the range ∼40 to ∼1200 K.

(iv) At a distance of 0.66 pc, there is a detached shell of optical thin ionized gas, which emits for free–free encounters. The ionized mass is ∼1.51 $M_\odot$ and the average density is 32 cm^{-3}.

(v) Almost co-spatial with the radio emission (Paper I), there is a component emitting in the mid-IR, which is very likely a result of line transitions (He II, [Ne II], [Ne III]) as found in this work. If a component of hot ($T \sim 340$–550 K) thermal dust is present, it has a negligible mass. We exclude the presence of non-thermal dust.

(vi) A component of warm ($T \sim 60$–85 K) grains is distributed in three concentric shells and has a total mass of ∼0.02 $M_\odot$ (in the case of mixed grains of silicate and graphite).

(vii) No cool dust is evident in the FIR images.

(viii) The IR spectra show the presence of a PDR, very likely distributed further out than the ionized region, but the considered data sets do not allow us to evaluate the contribution of the interstellar material. The electron density in the second shell is lower than ∼100 cm^{-3}, with the exception of the outer region in the north-east, where the density is higher (∼200 cm^{-3}). This region corresponds to the radio spur-emission, first detected by Higgs et al. (1994) and present also in our radio maps. The spectral index analysis of this region also gives evidence of the presence of density clumps. These clumps can be explained as a region modified by the impact of the ejecta with the local environment.

(ix) The gas-to-dust ratio in the nebula is $\approx 80 + (M_{\mathrm{neutral(M_\odot)}}/0.02)$.

The nebula morphology suggests that the star has lost mass in at least three different episodes. As already reported in Paper I, two of these occurred about 5.4×10^4 and 2.7×10^4 yr ago (assuming an expansion velocity of the shell of ∼30 km s^{-1}; Waters et al. 1996) and now we indicate an intermediate episode of 4.0×10^4 yr. Considering these epochs, the current mass loss does not explain the mass contained in the nebula. Assuming a linear expansion, this rate would have produced, in fact, a nebula with a mass of about a few 10^{-2} $M_\odot$ (i.e. two orders of magnitude less massive than the value determined from the observations). This implies that a higher mass-loss rate took place to form such a massive nebula and this is consistent with changes expected in the rate of mass loss for LBVs and observed in the case of AG Car.

After examining *IRAS* images, Waters et al. (1996) have reported that the nebulae were ejected with a mass-loss rate of $\sim 5 \times 10^{-4}$ $M_\odot$ yr^{-1}. By considering the nebular mass estimated in this work, we suggest instead a rate of $\sim 6.5 \times 10^{-5}$ $M_\odot$ yr^{-1}, which is consistent with many galactic LBVs. Mass-loss rates of the order of $\sim 10^{-5}$ $M_\odot$ yr^{-1} have been derived by Groh et al. (2009) for AG Car, by Najarro et al. (2009) for the Pistol star and FMM362 and by Clark et al. (2003) for G24.73+0.69. Higher mass-loss rates (greater than $\sim 10^{-4}$ $M_\odot$ yr^{-1}) have been determined for the more luminous η Car (Hillier et al. 2001), AFGL 2298 (Clark et al. 2009) and G26.47+0.02 (Umana et al. 2012). Lower mass-loss rates ($\sim 10^{-6}$ $M_\odot$ yr^{-1}) have also been observed in a few cases, such as W243 (Ritchie et al. 2009), Wra 17-96 (Egan et al. 2002) and HD162685 (Umana et al. 2010).

In the computation of the total nebular mass, we have not considered the contribution of the neutral gas. Therefore, our estimates of the nebular mass and the average mass-loss rate must be considered to be lower limits. However, the discrepancy with Waters et al. (1996) is probably mostly a result of the difference in the ionized mass determined in previous works with respect to our estimate. In fact, the mass determined in this work is at least four times smaller than the mass computed by Higgs et al. (1994). A massive nebula, such as proposed previously, would be comparable in mass to the Homunculus nebula around η Car, although G79.29+0.46 is less luminous, and consequently less massive, than η Car. While the difference between the high nebular mass around G79.29+0.46 and its initial mass would have fascinating implications for massive stellar evolution, the ejecta mass estimated in this work appears to be in agreement with a low-luminosity massive star.

G79.29+0.46 is still considered a cLBV because it does not match the variability criteria. However, indirect evidence for changes in the mass-loss rates has been pointed out. Indeed, it could be a LBV in the quiescent that has suffered at least three events of higher mass loss over the last 5.4×10^4 yr.

ACKNOWLEDGEMENTS

We thank the anonymous referee for useful comments that have helped to improve the manuscript. This paper is part of the PhD thesis of CA, who is very grateful to her tutors for supervising her PhD work. CA also thanks the *Spitzer* Science Center/Infrared Processing and Analysis Center staff at Caltech for the support provided during her visit to complete this project. She would especially like to thank Roberta Paladini for the invaluable suggestions received during her PhD programme.

This work is based on observations performed at the National Radio Astronomy Observatory, a facility of the National Science Foundation operated under cooperative agreement by Associated Universities, Inc. *Herschel* is a European Space Agency (ESA) space observatory with science instruments provided by the European-led Principal Investigator consortia and with important participation from the National Aeronautics and Space Administration (NASA). This research has also made use of the NASA/IPAC Infrared Science Archive, which is operated by the Jet Propulsion Laboratory, California Institute of Technology, under contract with NASA. The *ISO* was an ESA project with instruments funded by ESA Member States (especially the PI countries, France, Germany, the Netherlands and the UK) and with the participation of ISAS and NASA. Finally, this publication makes use of data products from the 2MASS, which is a joint project of the University of Massachusetts and the Infrared Processing and Analysis Center/California Institute of Technology, funded by NASA and the National Science Foundation.

REFERENCES

Albacete Colombo J. F., Flaccomio E., Micela G., Sciortino S., Damiani F., 2007, A&A, 464, 211
Bernard J.-P. et al., 2010, A&A, 518, L88
Chugai N. N., Danziger I. J., 2003, Astron. Lett., 29, 649
Clark J. S., Egan M. P., Crowther P. A., Mizuno D. R., Larionov V. M., Arkharov A., 2003, A&A, 412, 185
Clark J. S., Larionov V. M., Arkharov A., 2005, A&A, 435, 239
Clark J. S., Crowther P. A., Larionov V. M., Steele I. A., Ritchie B. W., Arkharov A. A., 2009, A&A, 507, 1555
Conti P. S., Frost S. A., 1976, BAAS, 8, 340
Dayal A., Hoffmann W. F., Bieging J. H., Hora J. L., Deutsch L. K., Fazio G. G., 1998, ApJ, 492, 603

Egan M. P., Clark J. S., Mizuno D. R., Carey S. J., Steele I. A., Price S. D., 2002, ApJ, 572, 288
Emerson D. T., Graeve R., 1988, A&A, 190, 353
Ferland G. J., Korista K. T., Verner D. A., Ferguson J. W., Kingdon J. B., Verner E. M., 1998, PASP, 110, 761
Flagey N., Boulanger F., Noriega-Crespo A., Paladini R., Montmerle T., Carey S. J., Gagné M., Shenoy S., 2011a, A&A, 531, A51
Flagey N., Noriega-Crespo A., Billot N., Carey S. J., 2011b, ApJ, 741, 4
Giannini T., Nisini B., Lorenzetti D., 2001, ApJ, 555, 40
Groh J. H., Hillier D. J., Damineli A., Whitelock P. A., Marang F., Rossi C., 2009, ApJ, 698, 1698
Gvaramadze V. V., Kniazev A. Y., Fabrika S., 2010, MNRAS, 405, 1047
Hanson M. M., 2003, ApJ, 597, 957
Higgs L. A., Wendker H. J., Landecker T. L., 1994, A&A, 291, 295
Hillier D. J., Davidson K., Ishibashi K., Gull T., 2001, ApJ, 553, 837
Hora J. et al., 2007, Spitzer Proposal ID 40184
Houck J. R., Shure M. A., Gull G. E., Herter T., 1984, ApJ, 287, L11
Humphreys R. M., Davidson K., 1994, PASP, 106, 1025
Izumiura H., Waters L. B. F. M., de Jong T., Loup C., Bontekoe T. R., Kester D. J. M., 1997, A&A, 323, 449
Jiménez-Esteban F. M., Rizzo J. R., Palau A., 2010, ApJ, 713, 429
Kotak R., Vink J. S., 2006, A&A, 460, L5
Kraemer K. E. et al., 2010, AJ, 139, 2319
Lamers H. J. G. L. M., Nota A., Panagia N., Smith L. J., Langer N., 2001, ApJ, 551, 764
Leitherer C., Robert C., 1991, ApJ, 377, 629
Mathis J. S., 1990, ARA&A, 28, 37
Mathis J. S., Rumpl W., Nordsieck K. H., 1977, ApJ, 217, 425
Mizutani M., Onaka T., Shibai H., 2002, A&A, 382, 610
Moorwood A. F. M., Baluteau J.-P., Anderegg M., Fitton B., Coron N., Biraud Y., 1980, ApJ, 238, 565
Morris P. W. et al., 1999, Nature, 402, 502
Morris P. W. Spitzer WRRINGS Team, 2008, in Bresolin F., Crowther P. A., Puls J., eds, Proc. IAU Symp. 250, Massive Stars as Cosmic Engines. Cambridge Univ. Press, Cambridge, p. 361
Najarro F., Figer D. F., Hillier D. J., Geballe T. R., Kudritzki R. P., 2009, ApJ, 691, 1816
Nazé Y., Rauw G., Hutsemékers D., 2012, A&A, 538, A47
Ofek E. O. et al., 2013, Nature, 494, 65
Paladini R. et al., 2012, ApJ, 760, 149
Panagia N., 1973, AJ, 78, 929
Panagia N., Felli M., 1975, A&A, 39, 1
Paradis D., Paladini R., Noriega-Crespo A., Lagache G., Kawamura A., Onishi T., Fukui Y., 2011, ApJ, 735, 6
Ritchie B. W., Clark J. S., Negueruela I., Najarro F., 2009, A&A, 507, 1597
Rizzo J. R., Jiménez-Esteban F. M., Ortiz E., 2008, ApJ, 681, 355
Schneider N., Bontemps S., Simon R., Jakob H., Motte F., Miller M., Kramer C., Stutzki J., 2006, A&A, 458, 855
Simpson J. P., Colgan S. W. J., Cotera A. S., Erickson E. F., Hollenbach D. J., Kaufman M. J., Rubin R. H., 2007, ApJ, 670, 1115
Smith N., Gehrz R. D., Hinz P. M., Hoffmann W. F., Hora J. L., Mamajek E. E., Meyer M. R., 2003, AJ, 125, 1458
Smith N. et al., 2007, ApJ, 666, 1116
Smith J. D. T., Rudnick L., Delaney T., Rho J., Gomez H., Kozasa T., Reach W., Isensee K., 2009, ApJ, 693, 713
Stahl O., Jankovics I., Kovács J., Wolf B., Schmutz W., Kaufer A., Rivinius T., Szeifert T., 2001, A&A, 375, 54
Tielens A. G. G. M., Hollenbach D., 1985, ApJ, 291, 722
Torres-Dodgen A. V., Carroll M., Tapia M., 1991, MNRAS, 249, 1
Trams N. R., Voors R. H. M., Waters L. B. F. M., 1998, Ap&SS, 255, 195
Trams N. R., van Tuyll C. I., Voors R. H. M., de Koter A., Waters L. B. F. M., Morris P. W., 1999, in Wolf B., Stahl O., Fullerton A. W., eds, Lecture Notes in Physics Vol. 523, Variable and Non-spherical Stellar Winds in Luminous Hot Stars. Springer, Berlin, p. 71
Umana G., Buemi C. S., Trigilio C., Hora J. L., Fazio G. G., Leto P., 2009, ApJ, 694, 697
Umana G., Buemi C. S., Trigilio C., Leto P., Hora J. L., 2010, ApJ, 718, 1036
Umana G., Buemi C. S., Trigilio C., Leto P., Agliozzo C., Ingallinera A., Noriega-Crespo A., Hora J. L., 2011, ApJ, 739, L11 (Paper I)
Umana G. et al., 2012, MNRAS, 427, 2975
Vamvatira-Nakou C., Hutsemékers D., Royer P., Nazé Y., Magain P., Exter K., Waelkens C., Groenewegen M. A. T., 2013, A&A, 557, A20
Van Dyk S. D., 2013, AJ, 145, 118
van Genderen A. M., 2001, A&A, 366, 508
van Loon J. T. et al., 2010, AJ, 139, 68
Vink J. S., de Koter A., 2002, A&A, 393, 543
Vink J. S., de Koter A., Kotak R., 2008a, in de Koter A., Smith L. J., Waters L. B. F. M., eds, ASP Conf. Ser. Vol. 388, Mass Loss from Stars and the Evolution of Stellar Clusters. Astron. Soc. Pac., San Francisco, p. 47
Vink J. S., Drew J. E., Steeghs D., Wright N. J., Martin E. L., Gänsicke B. T., Greimel R., Drake J., 2008b, MNRAS, 387, 308
Voors R. H. M., Geballe T. R., Waters L. B. F. M., Najarro F., Lamers H. J. G. L. M., 2000a, A&A, 362, 236
Voors R. H. M. et al., 2000b, A&A, 356, 501
Wachter S., Mauerhan J., van Dyk S., Hoard D. W., Morris P., 2011, Bull. Soc. R. Sci. Liège, 80, 291
Waters L. B. F. M., Izumiura H., Zaal P. A., Geballe T. R., Kester D. J. M., Bontekoe T. R., 1996, A&A, 313, 866
Wendker H. J., Molthagen K., Heske A., Higgs L. A., Landecker T. L., 1998, Ap&SS, 255, 187
Wright E. L. et al., 2010, AJ, 140, 1868

APPENDIX A: INFRARED SPECTRA

Figs A1 and A2 show the position of the *Spitzer* and *ISO* slits, respectively, superimposed on the 24-μm *Spitzer* image. Fig. A3 shows all the LWS spectra, taken at different positions on the nebula. Fig. A4 contains the most significant emission lines detected by the SWS positioned at the nebula's centre. The IRS background-subtracted spectra are shown in Fig. A5. Finally, Tables A1–A5 list the line flux measurements before and after the extinction correction.

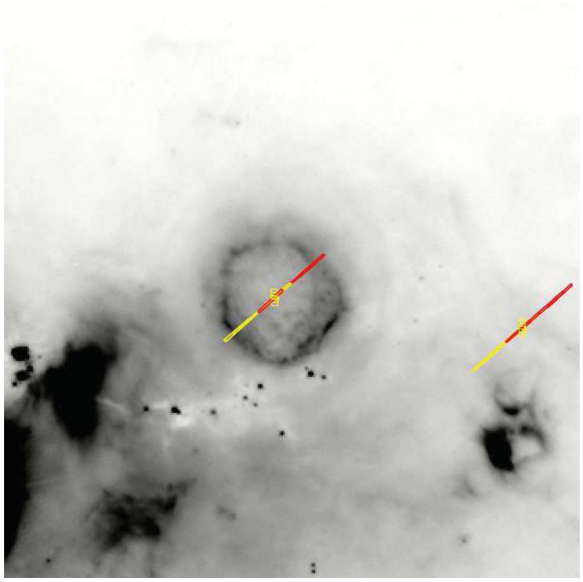

Figure A1. MIPS/*Spitzer* 24-μm image of G79.29+0.46 and the positions of the IRS SH and LH/*Spitzer* (centre) and IRS SL/*Spitzer* (nebula) slits.

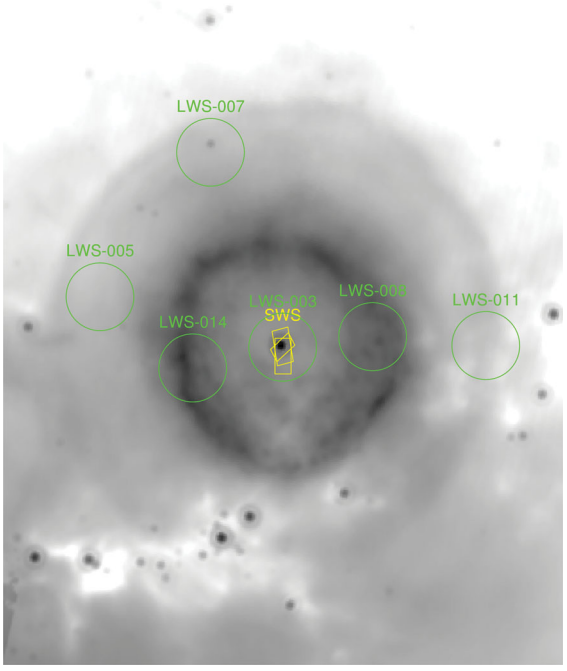

Figure A2. MIPS/*Spitzer* 24-μm image of G79.29+0.46 and the positions of the LWS/*ISO* (green) and SWS/*ISO* (yellow) slits.

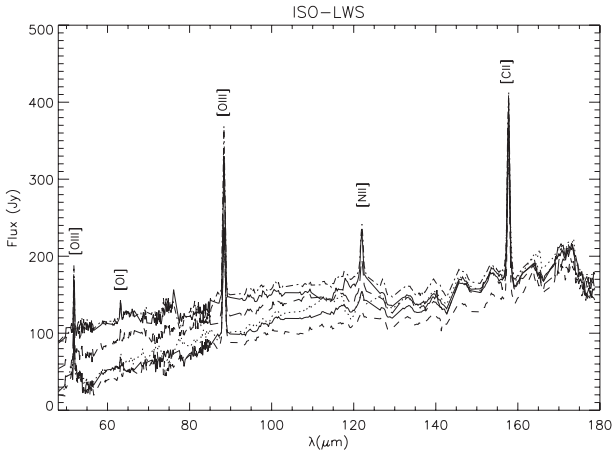

Figure A3. LWS spectra taken at six different positions on the nebula (three on the first shell and three on the second shell).

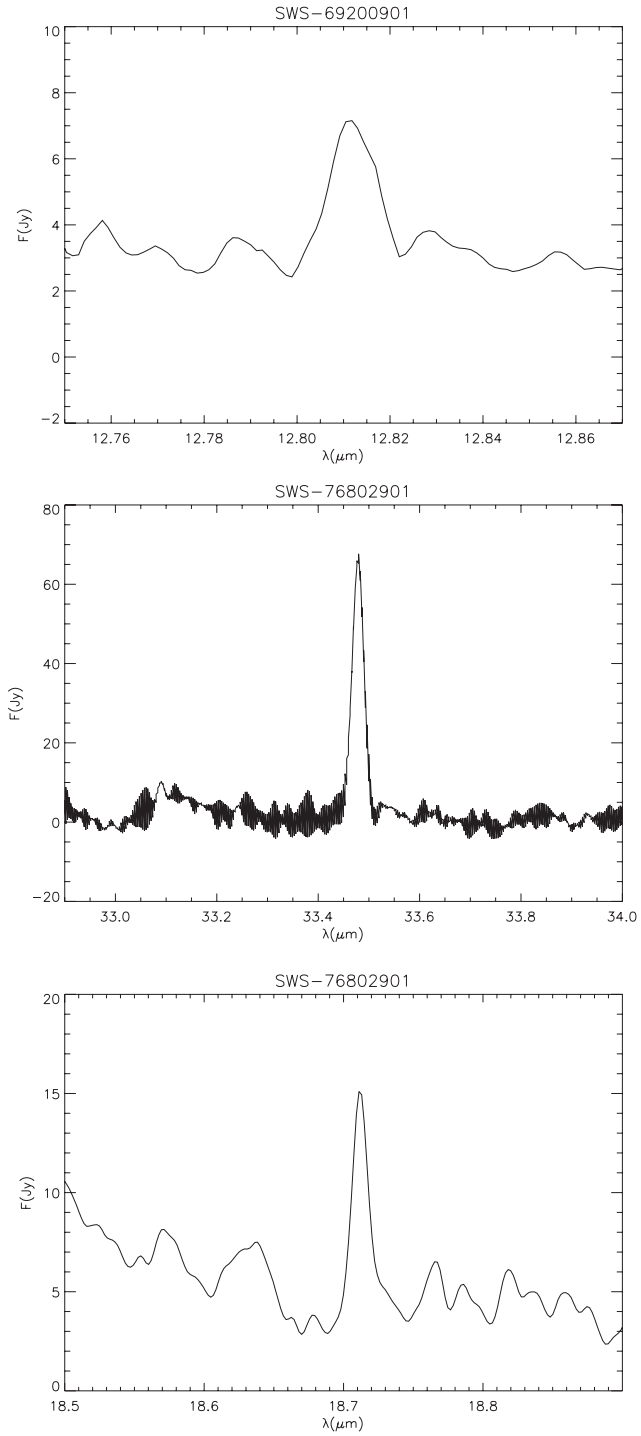

Figure A4. *ISO* SWS spectra taken on the star's position as shown in Fig. A2. We do not show the [Si II] 34.81-μm line because it is affected by fringing.

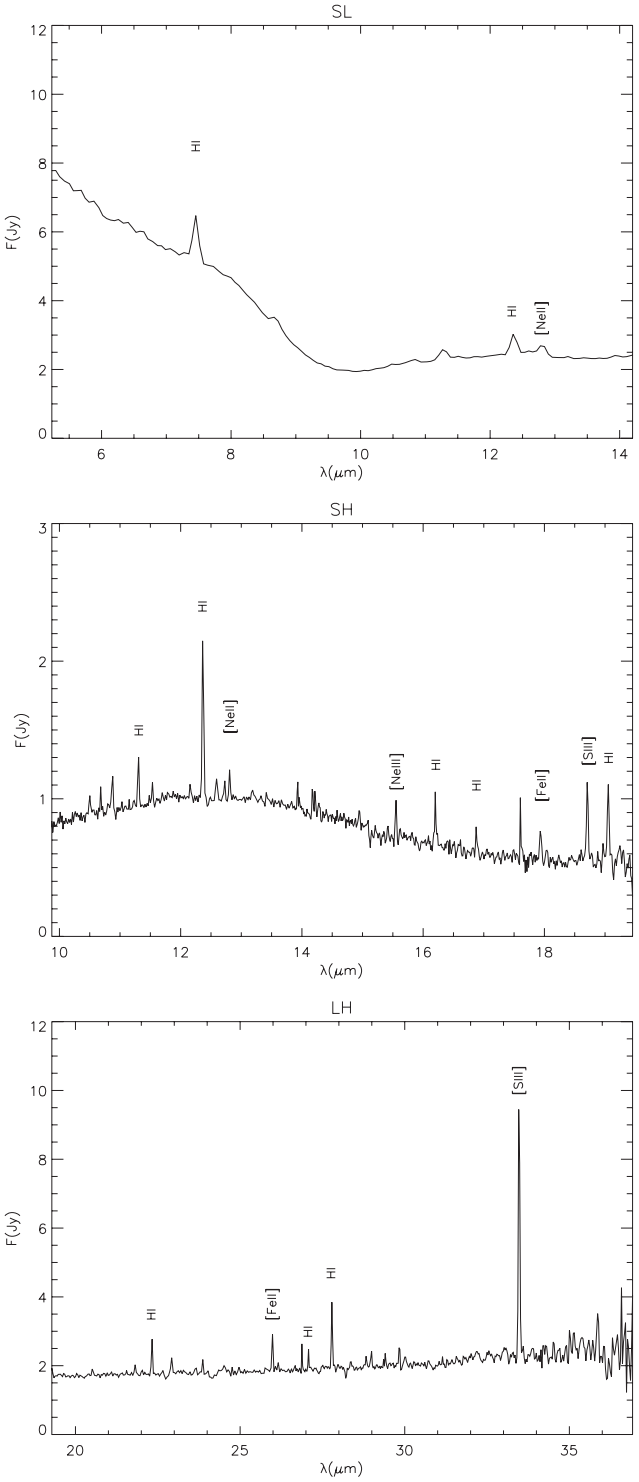

Figure A5. IRS SL (CH0), SH (CH1) and LH (CH3) spectra after the background subtraction. Data were taken on the star's position (SL and SH) and on the nebula (LH) as shown in Fig. A1.

Table A1. SWS line fluxes.

λ_{cent} (μm)	λ_{lab} (μm)	Element	Transition	$F_{observed}$ (10^{-19} W cm^{-2})	$F_{dereddened}$ (10^{-19} W cm^{-2})	No.
12.8121	12.8135	[Ne II]	2P(1/2)–2P(3/2)	1.05 ± 0.02	3.2 ± 0.4	sws69200901
18.7123	18.7130	[S III]	3P2–3P1	1.5 ± 0.1	4.6 ± 0.6	sws76802901
33.4780	33.4810	[S III]	3P1–3P0	5.4 ± 0.1	6.2 ± 0.2	sws76802901
34.8128	34.8152	[Si II]	2P(3/2)–2P(1/2)	1.3 ± 0.3	1.3 ± 0.1	sws51705105

Table A2. Line fluxes derived from the LWS spectra, obtained at six different positions of the slit on the nebula.

λ_{cent} (μm)	λ_{lab} (μm)	Element	Transition	$F_{observed}$ (10^{-19} W cm^{-2})	$F_{dereddened}$ (10^{-19} W cm^{-2})	No.
51.8333	51.8145	[O III]	3P2–3P1	20.1 ± 3.6	28.2 ± 4.8	lws35801011
51.8191				30.8 ± 4.4	55 ± 5	lws35801007
51.7381				38.7 ± 5.5	46 ± 6	lws35801005
51.8234				29.6 ± 2.4	32.6 ± 3.7	lws35801014
51.8471				26 ± 2	28.5 ± 3.1	lws35801008
51.8221				34.4 ± 3.4	38.8 ± 3.4	lws35801003
63.1785	63.1837	[O I]	(3P1–3P2)	4.6 ± 0.8	4.6 ± 1.4	lws35801011
63.1785				3.9 ± 0.3	3.3 ± 1.8	lws35801007
63.2027				3.7 ± 0.8	4.1 ± 1.1	lws35801005
63.1774				5.1 ± 1.2	5.3 ± 1.1	lws35801014
63.1734				5.3 ± 1.8	5.4 ± 2.0	lws35801008
63.1870				3.3 ± 0.3	4.7 ± 2.3	lws35801003
88.4118	88.3560	[O III]	(3P1–3P0)	40.8 ± 2.7	42 ± 3	lws35801011
88.3803				43.05 ± 1.46	47.7 ± 5.7	lws35801007
88.3960				35 ± 2	37.2 ± 3.6	lws35801005
88.3734				59.4 ± 5.1	61.5 ± 6.1	lws35801014
88.4099				51.2 ± 1.8	51.7 ± 4.2	lws35801008
88.3817				52.2 ± 1.1	53 ± 3	lws35801003
122.1056	121.898	[N II]	(3P2–3P1)	8 ± 1	8.4 ± 2.3	lws35801011
122.0106				3.6 ± 1.2	4.4 ± 1.5	lws35801007
121.6556				4.7 ± 1.7	5.1 ± 1.8	lws35801005
121.9799				12.5 ± 1.5	12.9 ± 2.2	lws35801014
121.9589				14.2 ± 2.5	15 ± 2	lws35801008
121.9886				8.79 ± 0.76	10.0 ± 1.6	lws35801003
157.7338	157.741	[C II]	2P(3/2)–2P(1/2)	17.6 ± 0.1	18.1 ± 2.2	lws35801011
157.7237				15.01 ± 0.35	15.2 ± 1.7	lws35801007
157.7191				18.0 ± 1.5	18.6 ± 1.6	lws35801005
157.7185				20.2 ± 0.6	20.7 ± 1.6	lws35801014
157.7289				18.7 ± 1.2	19.9 ± 2.8	lws35801008
157.7207				17.2 ± 0.4	17.5 ± 1.7	lws35801003

Table A3. Line fluxes derived from the IRS/SL spectrum, after the background subtraction.

λ_{lab} (μm)	λ_{cent} (μm)	Element	Transition	$F_{observed}$ (10^{-21} W cm^{-2})	$F_{dereddened}$ (10^{-21} W cm^{-2})
7.4568	7.4526	He II	12–10	962 ± 160	$(2.5 \pm 1.4) \times 10^3$
12.2485	12.3635	He II	25–17	118.9 ± 29.6	485.7 ± 23.3
12.8135	12.8070	[Ne II]	2P(1/2)–2P(3/2)	82.9 ± 10.7	135.3 ± 105.8

Table A4. Line fluxes derived from the IRS/SH spectrum, after the background subtraction.

λ_{lab} (μm)	λ_{cent} (μm)	Element	Transition	$F_{observed}$ (10^{-21} W cm^{-2})	$F_{dereddened}$ (10^{-21} W cm^{-2})
11.3026	11.3025	H I (He II)	23–16 (18–14)	27.8 ± 5.6	165.3 ± 39.9
12.3669	12.3677	H I (He II)	14–12 (7–6)	65.4 ± 14.0	275.5 ± 17.7
12.8135	12.8086	[Ne II]	2P1/2–2P3/2	9.9 ± 1.5	40.0 ± 13.0
15.5551	15.5511	[Ne III]	3P1–3P2	11.6 ± 3.4	17.9 ± 3.2
16.2025	16.2009	H I	10–8	10.1 ± 2.2	24.0 ± 3.6
16.8737	16.8760	H I	12–9	4.3 ± 1.1	13.2 ± 3.7
17.9359	17.9358	[Fe II]	a4F7/2–a4F9/2	8.1 ± 2.2	24.9 ± 7.0
18.7130	18.7085	[S III]	3P2–3P1	14.8 ± 1.8	45.6 ± 6.1
19.0541	19.0527	H I	8–7	15.5 ± 3.6	46.9 ± 10.1

Table A5. Line fluxes derived from the IRS/LH spectrum, after the background subtraction.

λ_{lab} (μm)	λ_{cent} (μm)	Element	Transition	$F_{observed}$ (10^{-21} W cm^{-2})	$F_{dereddened}$ (10^{-21} W cm^{-2})
22.3316	22.3191	H I (He II)	13–10 (22–18)	24.5 ± 7.7	61.9 ± 14.2
25.9883	25.9758	[Fe II]	a6D7/2–a6D9/2	24.1 ± 2.9	42.4 ± 15.2
27.0880	27.0756	H I	24–14	7.2 ± 1.5	13.3 ± 5.3
27.7921	27.7887	H I	9–8	30.7 ± 3.3	54.6 ± 7.1
33.4810	33.4729	[S III]	3P1–3P0	109.9 ± 6.3	146.5 ± 5.4

This paper has been typeset from a TEX/LATEX file prepared by the author.